Draft, 20101010
Preprint typeset using LaTeX style emulateapj v. 11/10/09

arXiv:1003.4990v3 [astro-ph.CO] 15 Dec 2010

RADIATIVE TRANSFER MODELING OF LYMAN ALPHA EMITTERS. II. NEW EFFECTS IN GALAXY CLUSTERING

Zheng Zheng[1], Renyue Cen[2], Hy Trac[3,4], and Jordi Miralda-Escudé[5,6]

Draft, 20101010

ABSTRACT

We study the clustering properties of $z \sim 5.7$ Lyα emitters (LAEs) in a cosmological reionization simulation with a full Lyα radiative transfer calculation. Lyα radiative transfer substantially modifies the intrinsic Lyα emission properties, compared to observed ones, depending on the density and velocity structure environment around the Lyα -emitting galaxy. This environment-dependent Lyα selection introduces new features in LAE clustering, suppressing (enhancing) the line-of-sight (transverse) density fluctuations and giving rise to scale-dependent galaxy bias. In real space, the contours of the three-dimensional two-point correlation function of LAEs appear to be prominently elongated along the line of sight on large scales, an effect that is opposite to and much stronger than the linear redshift-space distortion effect. The projected two-point correlation function is greatly enhanced in amplitude by a factor of up to a few, compared to the case without the environment-dependent selection effect. The new features in LAE clustering can be understood with a simple, physically motivated model, where Lyα selection depends on matter density, velocity, and their gradients. We discuss the implications and consequences of the effects on galaxy clustering from Lyα selection in interpreting clustering measurements and in constraining cosmology and reionization from LAEs.

Subject headings: cosmology: observations — galaxies: halos — galaxies: high-redshift — galaxies: statistics — intergalactic medium — large-scale structure of universe — radiative transfer — scattering

1. INTRODUCTION

Lyα emitters (hereafter LAEs) are galaxies with strong Lyα emission lines. Owing to the strong Lyα line feature, LAEs can be efficiently detected through narrowband imaging or with integral-field-units (IFU) spectroscopy, which makes them natural targets for searches of high-redshift galaxies. Large samples of high-redshift LAEs are expected with ongoing and forthcoming LAE surveys. In this paper, we investigate the clustering of $z \sim 5.7$ LAEs in a cosmological reionization simulation, focusing on the effects of Lyα radiative transfer on their clustering properties.

Large samples of LAEs would provide exciting opportunities to probe the high redshift universe. The resonance nature of Lyα line makes LAEs a sensitive probe of the high-redshift intergalactic medium (IGM), especially across the reionization epoch (e.g., Miralda-Escudé & Rees 1998; Miralda-Escudé 1998; Haiman & Spaans 1999; Santos 2004; Haiman & Cen 2005; Wyithe & Cen 2007; Malhotra & Rhoads 2004; Kashikawa et al. 2006; Furlanetto et al. 2006; Dijkstra, Lidz, & Wyithe 2007; Dijkstra, Wyithe, & Haiman 2007; McQuinn et al. 2007; Mesinger & Furlanetto 2008; Iliev et al. 2008; Dayal et al. 2008, 2009, 2010). In particular, the clustering of LAEs at redshift $z > 6$ can potentially put tight constraints on the ionization status of the IGM (e.g., Furlanetto et al. 2006; McQuinn et al. 2007; Iliev et al. 2008).

Large samples of LAEs should enable accurate measurements of their clustering. As with galaxy clustering in general, the clustering of LAEs encodes useful information of galaxy formation and evolution. We expect to learn about the relation between these young galaxies and dark matter halos, and to obtain insights on the early stage of structure formation.

Galaxy clustering also encodes important cosmological information. The fluctuation power spectrum of galaxies is related to that of matter, usually differing by a constant, multiplicative galaxy bias factor on large scales. Because nonlinearity is weaker at higher redshift, the galaxy power spectrum may be used down to smaller spatial scales for constraining cosmology, tightening constraints on parameters like the neutrino mass and providing tests of inflation (e.g., Takada et al. 2006). The efficient detection of LAEs at high redshift makes them attractive candidates in this endeavor. Large-volume surveys of LAEs, such as the Hobby–Eberly Telescope Dark Energy Experiment (Hill et al. 2008), might also enable the detection of the baryon acoustic oscillations feature (e.g., Eisenstein et al. 2005) in the LAE power spectrum. Baryon acoustic oscillations can be used to measure the expansion history of the universe, contributing to constraints on the evolution of dark energy and the curvature of the universe.

At present, measurements of LAEs clustering are very limited by small survey volumes and small samples of LAEs. Ouchi et al. (2003) present the angular two-point

---

[1] Yale Center for Astronomy and Astrophysics, Yale University, New Haven, CT 06520; zheng.zheng@yale.edu
[2] Department of Astrophysical Sciences, Princeton University, Peyton Hall, Ivy Lane, Princeton, NJ 08544
[3] Harvard-Smithsonian Center for Astrophysics, Cambridge, MA 02138
[4] Department of Physics, Carnegie Mellon University, Pittsburgh, PA 15213
[5] Institució Catalana de Recerca i Estudis Avançats, Barcelona, Catalonia
[6] Institut de Ciències del Cosmos, Universitat de Barcelona, Barcelona, Catalonia

correlation function (hereafter, 2PCF) of 87 $z = 4.86$ LAEs in a 0.15deg^2 narrowband survey in the Subaru Deep Field. The correlation length is estimated to be $(3.5 \pm 0.3)h^{-1}$Mpc (and $(6.2 \pm 0.5)h^{-1}$Mpc if a maximum contamination correction is applied), larger than that of $z \sim 4$ Lyman break galaxies. With a set of LAEs found in a larger area ($\sim$0.3 deg^2) around the same field, Shimasaku et al. (2004) also report strong clustering for 41 $z = 4.86$ LAEs, but they find almost no clustering for 51 $z = 4.79$ LAEs. The strong clustering of $z = 4.86$ LAEs is difficult to reproduce with a simple model that relates LAEs to dark matter halos (Hamana et al. 2004). With 151 $z = 4.5$ LAEs in a 0.36deg^2 field of the narrowband Large Area Lyman Alpha (LALA) survey, Kovač et al. (2007) estimate a correlation length of $3.2 \pm 0.4h^{-1}$Mpc ($4.6 \pm 0.6h^{-1}$Mpc with contamination correction). The clustering can be reproduced if these LAEs reside in halos more massive than (1–2)$\times 10^{11}h^{-1}M_\odot$. Gawiser et al. (2007) measure the angular 2PCF of 162 $z = 3.1$ LAEs discovered in a 0.28deg^2 field of the MUltiwavelength Survey by Yale-Chile (MUSYC). They find a moderate clustering with a correlation length of $2.5^{+0.6}_{-0.7}h^{-1}$Mpc, corresponding to that of halos with a minimum mass of $\sim 2.8 \times 10^{10}h^{-1}M_\odot$ (and a median mass of $5.6 \times 10^{10}h^{-1}M_\odot$). The 261 $z = 2.1$ LAEs in the same MUSYC field have a correlation length of $3.2 \pm 0.6h^{-1}$Mpc (Guaita et al. 2010), corresponding to a median halo mass of $1.8 \times 10^{11}h^{-1}M_\odot$. From the clustering of $z = 3$–7 LAEs in the 1deg^2 Subaru/*XMM-Newton* Deep Survey (SXDS), Ouchi et al. (2010) infer that the average host halo mass is 10^{10}–$10^{11}M_\odot$. Understanding the LAE clustering results needs to take into account the differences in LAE samples and redshifts, as well as sample variance caused by small survey volumes. The development of a physically based theoretical model of LAEs and their clustering is also needed.

In models of LAEs, the Lyα flux of an LAE is usually computed from the emitted ionizing photons in the galaxy residing in a dark matter halo, assuming Case B recombination (Osterbrock 1989). The theoretical modeling of LAE clustering depends on how LAEs and dark matter halos are connected, and how the observed Lyα luminosity is determined from the intrinsic Lyα luminosity. Generally speaking, there are two scenarios considered in LAE models, the duty cycle scenario and the Lyα escape fraction scenario. In the duty cycle scenario, LAEs are short-lived and at any given time only a fraction of all galaxies are active as LAEs. In the Lyα escape fraction scenario, it is assumed that only a fraction of Lyα photons can escape from the source, and therefore the observed Lyα luminosity is a fraction of the intrinsic one. Either scenario can make the predicted Lyα luminosity function (LF) match the observation. For a given number density of LAEs, the masses of host halos in the duty cycle scenario would be on average lower than those in the escape fraction scenario. As a consequence, the clustering of LAEs would be different in the two scenarios, with a stronger clustering in the escape fraction scenario.

Nagamine et al. (2010) predict LAE clustering based on cosmological smoothed particle hydrodynamic (SPH) simulation and consider both scenarios. They find that LAE clustering measurements from observations are in favor of their duty cycle scenario. Tilvi et al. (2009) present an LAE model in which Lyα luminosity or star formation rate (SFR) is related to the halo mass accretion rate, rather than halo mass, and the model naturally gives rise to the duty cycle of LAEs. Their model predict correlation lengths of LAEs in agreement with the observations. Orsi et al. (2008) combine a semi-analytic model of galaxy formation with a large N-body simulation to predict the clustering of LAEs. They adopt the scenario of Lyα escape fraction and assume the escape fraction to be constant (2%) and independent of galaxy properties. By accounting for the large sample variance, the model is found to reproduce the angular clustering measurements from current surveys of LAEs. McQuinn et al. (2007) develop a model of LAEs using reionization simulations with cosmological volume (see also Iliev et al. 2008) and discuss the effect of reionization on LAE clustering. Their model computes the escape fraction based on a simplified treatment of Lyα radiative transfer (hereafter, RT) that consists of multiplying the intrinsic line profile by $\exp(-\tau_\nu)$, where τ_ν is the optical depth at frequency ν along the line of sight. The $\exp(-\tau_\nu)$ model is reasonably accurate in the case of studying the absorption feature of Lyα photons passing through some neutral regions along the line of sight, especially for absorption caused by the damping wing or small optical depth. For studying the observed Lyα emission, the model is not accurate. Even if one limits the $\exp(-\tau_\nu)$ model to study the transfer outside of a radius much larger than halo size by assuming a Lyα line profile at that radius, it is not clear what radius to use, what line profile to assume, and what angular distribution of Lyα emission at that radius to adopt. The model neglects the spatial and frequency diffusion of Lyα photons, which is important because of the scattering, not the absorption nature of the transfer of Lyα photons.

Zheng et al. (2010) (hereafter Paper I) present a simple physical model of LAEs, where Lyα RT is the primary physical process transforming intrinsic Lyα emission properties to observed ones. For the first time, a full RT calculation of Lyα photons (Zheng & Miralda-Escudé 2002) in gas halos around LAEs is performed in a self-consistent fashion with the radiation-hydrodynamic reionization simulations (Trac et al. 2008). While in this model the number of Lyα photons in the IGM is correctly conserved, only a fraction of them can be observed, those included in the central part of the extended Lyα emission with high enough surface brightness. The model predicts a broad distribution of apparent (observed) Lyα luminosity at fixed intrinsic Lyα luminosity or ultraviolet (UV) luminosity, a consequence of a variable intergalactic environment of LAEs and the environment-dependent RT of Lyα photons. Therefore, the model predicts an effective Lyα escape fraction that is not constant, but has a broad distribution and is correlated with the environment. This simple physical model is able to explain an array of observed properties of $z \sim$5.7 LAEs in Ouchi et al. (2008), including Lyα spectra, morphology, and apparent Lyα LF. The broad distribution of apparent Lyα luminosity at fixed UV luminosity provides a natural explanation for the observed UV LF, especially the turnover toward the low-luminosity end. The model also reproduces the observed distribution of Lyα equivalent width (EW) and explains the deficit of UV bright, high-EW sources.

In this paper, we investigate the clustering of LAEs within the model presented in Paper I. As we will show, the environment-dependent Lyα RT introduces new and significant effects in the clustering of galaxies selected by Lyα emission, a real physical effect that has not been properly taken into account in previous studies. We first present the environment dependence of the Lyα selection and the dependence on halo mass in Section 2. In Section 3, we present the results of LAE clustering from our model, in terms of the 2PCFs. Following an intuitive interpretation of the features seen in LAE clustering, we provide a simple physical model to further aid our understanding of LAE clustering. In Section 4, we show the environment dependence of the halo occupation distribution (HOD) of LAEs. In Section 5, we summarize our main findings and discuss the implications. In the appendices, we provide an extended simple physical model of LAE clustering, present the power spectrum of LAEs, make comparisons to the LAE clustering in the $\exp(-\tau_\nu)$ model, and present tests on factors that may mask the new clustering effects.

Throughout the paper, we adopt the same cosmological model as in the reionization simulation (Trac et al. 2008) used in our RT calculation. It is a spatially flat ΛCDM cosmological model with Gaussian initial density fluctuations, and the cosmological parameters are consistent with the *Wilkinson Microwave Anisotropy Probe* 5 year data (Dunkley et al. 2009): $\Omega_m = 0.28$, $\Omega_\Lambda = 0.72$, $\Omega_b = 0.046$, $h = 0.70$, $n_s = 0.96$, and $\sigma_8 = 0.82$. Our Lyα RT calculation is based on the $z = 5.7$ output of the simulation, which has a box size of $100h^{-1}$Mpc on a side. In our calculation, a 768^3 grid is used to represent the neutral hydrogen density, temperature, and peculiar velocity fields in the simulation box. The Hubble flow is added to the velocity field. LAEs are assumed to reside in dark matter halos with positions and velocities from the halo catalog. To reduce source blending in the Lyα image and spectra, Lyα photons are collected with a finer spatial resolution, a 6144^2 grid for the image of the whole box, corresponding to $16.3h^{-1}$kpc (comoving) or $0.58''$per pixel. The spectral resolution and range are 0.1Å$(25\mathrm{km\,s^{-1}})$ and 24Åin rest frame, respectively. We divide the whole simulation box into three layers so that the depth of each layer approximates that from the width of the narrowband filter used in searching for $z \sim 5.7$ LAEs (Ouchi et al. 2008). The calculation result for each layer is saved in an IFU-like datacube of dimension 6144×6144×240. We refer the readers to Paper I for more details about the characteristics of the simulation and calculation.

2. ENVIRONMENT DEPENDENCE OF Lyα RADIATIVE TRANSFER

As shown in Paper I, a point Lyα -emitting source becomes extended in the end as a result of spatial diffusion caused by Lyα RT. Only the central, high surface brightness part of the extended source can be observed as an LAE. Therefore, the observed or apparent Lyα luminosity ($L_{\rm apparent}$) is reduced with respect to the intrinsic Lyα luminosity ($L_{\rm intrinsic}$). The suppression of Lyα emission, characterized by the ratio of observed to intrinsic Lyα luminosity, depends on the environments in the vicinities of LAEs. The environments here are interpreted broadly as the matter density and peculiar velocity. In Paper I, we identify a few environment variables. In general, the suppression is weaker in regions of lower density; the suppression depends on the sign of the density gradient along the line of sight, in the sense that sources located in the near side (with respect to the observer) of an overdense region have a lower suppression; relative to the Hubble flow, sources moving away from the observer have a lower suppression because of the additional redshift in Lyα frequency; sources with larger line-of-sight gradient of the line-of-sight peculiar velocity are more easily observed because of an effectively larger Hubble expansion rate.

In Figure 1, we show the environmental dependence of Lyα RT outcome in terms of the observed-to-intrinsic Lyα luminosity as a function of four physical variables — overdensity δ, its gradient along the line of sight, line-of-sight halo velocity, and peculiar velocity gradient along the line of sight, separately for four subsets of halos divided according to their halo mass. The overdensity field is smoothed with a three-dimensional (hereafter, 3D) top-hat filter of radius $2h^{-1}$Mpc (comoving). It is seen that the overall dependence becomes weaker for sources in halos of higher mass, probably indicating that Lyα scatterings encountered in virialized regions or their immediate surroundings, which are less affected by environments, becomes more important for higher mass halos.

Gravitational evolution of the cosmic structure leads to correlations among the above environment variables, which complicates the isolation of the role of each variable on the Lyα RT. To have a better understanding of the interplay of different environment variables, we study in detail the joint dependence of Lyα RT on two variables, the matter density and the line-of-sight velocity gradient, which appear to be the major factors in the effects shown in the clustering of LAEs (as discussed in the following section).

The gray scale in Figure 2 shows the joint distribution of local matter overdensity δ and $\partial v_z/\partial z$ for halos of mass $\sim 10^{10}h^{-1}M_\odot$. Clearly, the two quantities are anti-correlated: $\partial v_z/\partial z$ is, on average, larger (i.e., less negative) in less dense region, albeit with a large dispersion, which means that there is an effective higher Hubble constant in less dense regions than in higher density regions. This is easily understood using linear theory, where the linear velocity field is related to overdensity by $\delta \propto -\nabla \cdot \mathbf{v}$ from the continuity equation. Therefore, on average or in the spherical case, a higher density corresponds to a lower value of velocity gradient. Complex non-spherical geometry of density perturbations around sources causes the large dispersion seen in the correlation.

At each position in this $\partial v_z/\partial z$–δ plane, we compute the median value of the ratio of the observed to intrinsic Lyα luminosity. The contours show the distribution of the median ratio, with thicker contours for higher values. In the model with full Lyα RT calculation (left panel), at a fixed velocity gradient, Lyα luminosity appears to be *less* suppressed in regions of *higher* density. This may appear to be counter-intuitive and in contradiction with Figure 1(a). Naively, we expect more Lyα scatterings and larger spatial diffusion in denser regions, which would lower the ratio of observed-to-intrinsic Lyα lumi-

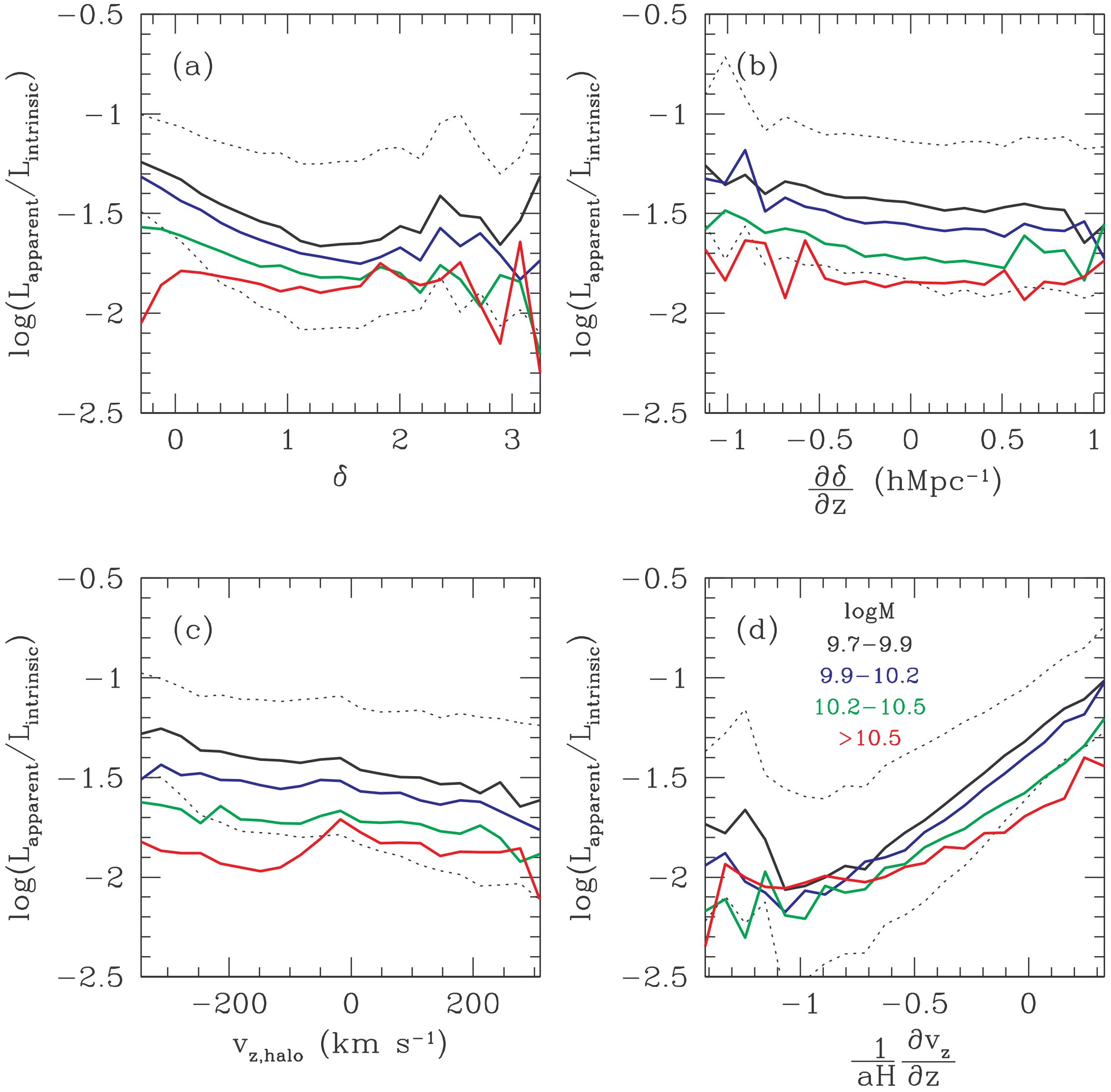

Fig. 1.— Dependence of Lyα flux suppression of LAEs on density and peculiar velocity, as a function of halo mass. The suppression is characterized by the ratio of the apparent (observed) and intrinsic Lyα luminosity $L_{\rm apparent}/L_{\rm intrinsic}$. (a) Dependence on the smoothed overdensity field at the source position. The overdensity field is smoothed with a 3D top-hat filter of radius $2h^{-1}$Mpc (comoving). (b) Dependence on the density gradient along the Z-direction. The derivative is with respect to comoving coordinate. (c) Dependence on the host halo velocity. (d) Dependence on the linear peculiar velocity gradient along the Z-direction. The linear peculiar velocity is obtained from the smoothed overdensity field based on the continuity equation (see the text for details). The velocity gradient is put in units of the Hubble parameter. Different colors are for LAE host halos of different masses, as labeled in panel (*d*). The median of the ratio is plotted as a solid curve. The two dotted curves delineate the upper and the lower quartiles, and for clarity we only plot those for the lowest mass range. Note that the line-of-sight direction (from the observer to sources) is along the $-Z$-direction, which matters for interpreting the results in panels (*b*) and (*c*). See Section 2 for further discussion.

nosity. This is opposite to what is seen in Figure 2, which implies that the density effect is masked by a stronger effect.

To understand this, we need to note that the linear velocity field is related to overdensity, $\delta \propto -\nabla\cdot\mathbf{v} = -(\partial v_x/\partial x + \partial v_y/\partial y + \partial v_z/\partial z)$. Therefore, at fixed $\partial v_z/\partial z$ a higher density corresponds to lower values of velocity gradients in the transverse directions. Since velocity gradient is dominant in determining observed-to-intrinsic Lyα luminosity ratio (see Section 7 in Paper I), lower values of velocity gradients in the transverse directions indicate a lower probability for Lyα photons to escape along the transverse directions. This is expected from the Lyα RT — we can think of this as that the scatterings of Lyα photons enable them to probe the optical depth in all directions and they prefer to travel the path with the least resistance.

Figure 3 gives a schematic illustration of the dependence of Lyα RT on the surroundings. Lyα photons are emitted from a central source (marked as a star in each panel). The gray scale of the ring around the source indicates Lyα optical depth in each direction, darker for higher optical depth. Scatterings of Lyα photons tend to make them escape in directions with lowest optical depth, leading to higher flux in these directions. The lengths of arrows illustrate the magnitude of flux in each

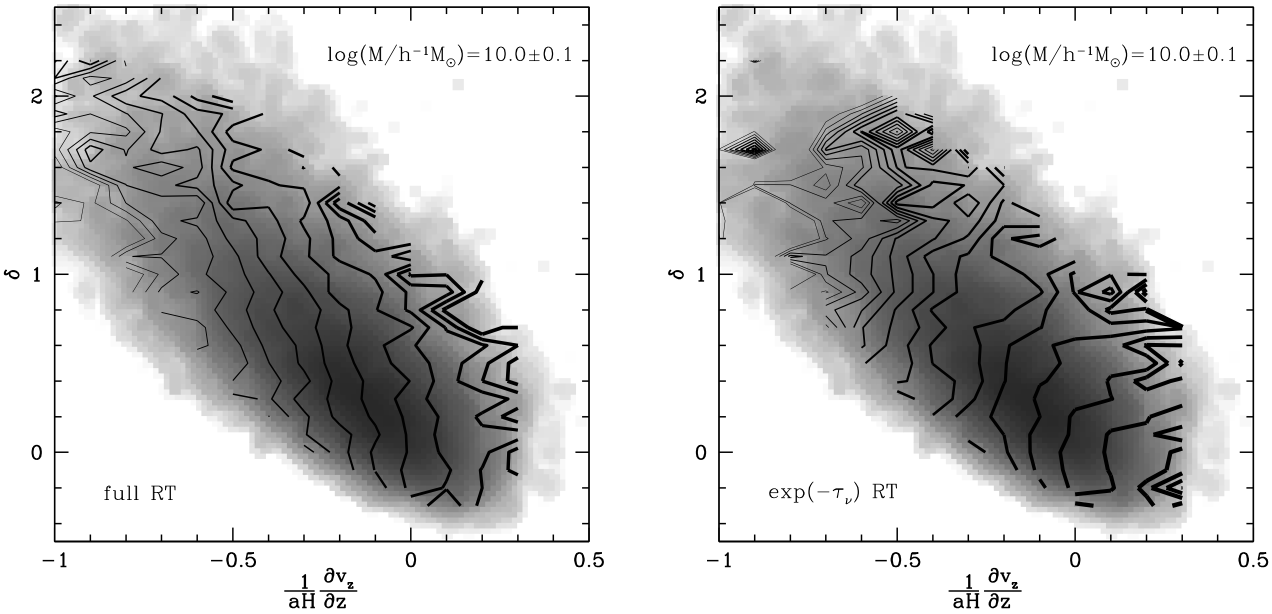

FIG. 2.— Joint dependence of Lyα flux suppression of LAEs on environments in the full Lyα RT model (left) and the $\exp(-\tau_\nu)$ model (right). In each panel, the gray scale shows the distribution of halos ($\sim 10^{10}h^{-1}M_\odot$) in the plane of density and line-of-sight velocity gradient, darker for higher probability density. Contours indicate the median Lyα flux suppression, defined as the ratio of observed to intrinsic Lyα luminosity, for LAEs residing in these halos. Thicker contours correspond to higher ratios, and adjacent contours differ by 0.1 dex in contour levels. Note the difference in the trend of flux ratios at fixed velocity gradient in the two models. See the text for details.

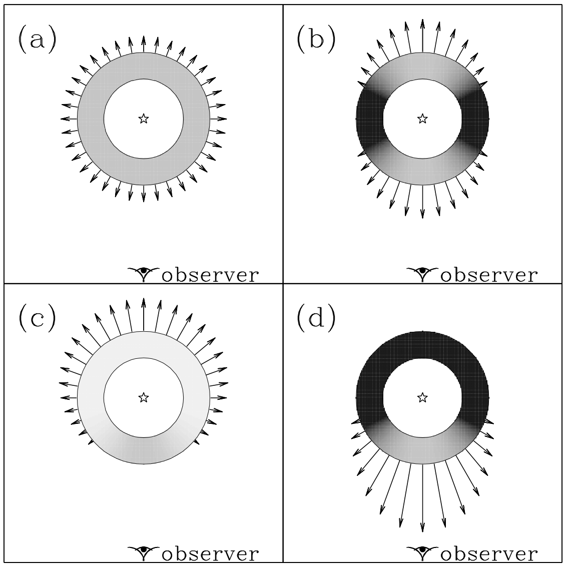

FIG. 3.— Schematic illustration of RT effect on the observed flux of Lyα emission. In each panel, Lyα photons are emitted from the central source and scattered by neutral gas surrounding it. The gas is shown as the shaded region, and the gray scale indicates the Lyα optical depth along each radial direction with darker for higher optical depth. The flux of escaped Lyα photons along each direction is illustrated by the arrows with length proportional to flux. Although the optical depths along the line-of-sight direction (from the observer to the source) are the same in all four panels, we expect to have different observed flux because of different distribution of optical depth in other directions.

direction. Although the line-of-sight optical depth is the same and the total flux over all directions is the same in the four cases shown in Figure 3, the observed fluxes are not. For example, in panel (d), the optical depths are high in directions other than the line-of-sight direction, and Lyα photons are all likely to be reflected toward the observer. While in panel (c), the optical depths are low in directions other than the line-of-sight direction, and the observer can only see a very low flux of Lyα photons. *The observed flux is therefore not purely determined by the line-of-sight optical depth, but the line-of-sight optical depth relative to those in all other directions.* This is a fundamental difference between the $\exp(-\tau_\nu)$ model and the full Lyα RT model, with the former only using the line-of-sight information. In the $\exp(-\tau_\nu)$ model, at fixed line-of-sight velocity gradient, the optical depth should increase with density, which is opposite to the full RT model and is seen in the right panel of Figure 2. The relative amplitude of the optical depth is the zeroth-order, primary effect on the directional propagation of Lyα photons. Of course, the overall amplitude of the optical depth (e.g., in the spherically symmetric case) determines the spatial extent of the Lyα photon diffusion and the overall degree of suppression of the observed Lyα luminosity.

While at fixed $\partial v_z/\partial z$ the observed-to-intrinsic Lyα luminosity ratio increases with density, it decreases with density if averaged over environments, as seen in Figure 1(a). The apparent contradiction is resolved by noticing that the latter is driven by the strong dependence of the Lyα luminosity ratio on $\partial v_z/\partial z$ (Figure 1(d) and the anti-correlation between density and $\partial v_z/\partial z$ (gray scale in Figure 2).

To have a visual impression of the environmental dependence of Lyα flux suppression in the simulation, we show a slice ($5h^{-1}$Mpc thick) of the spatial dis-

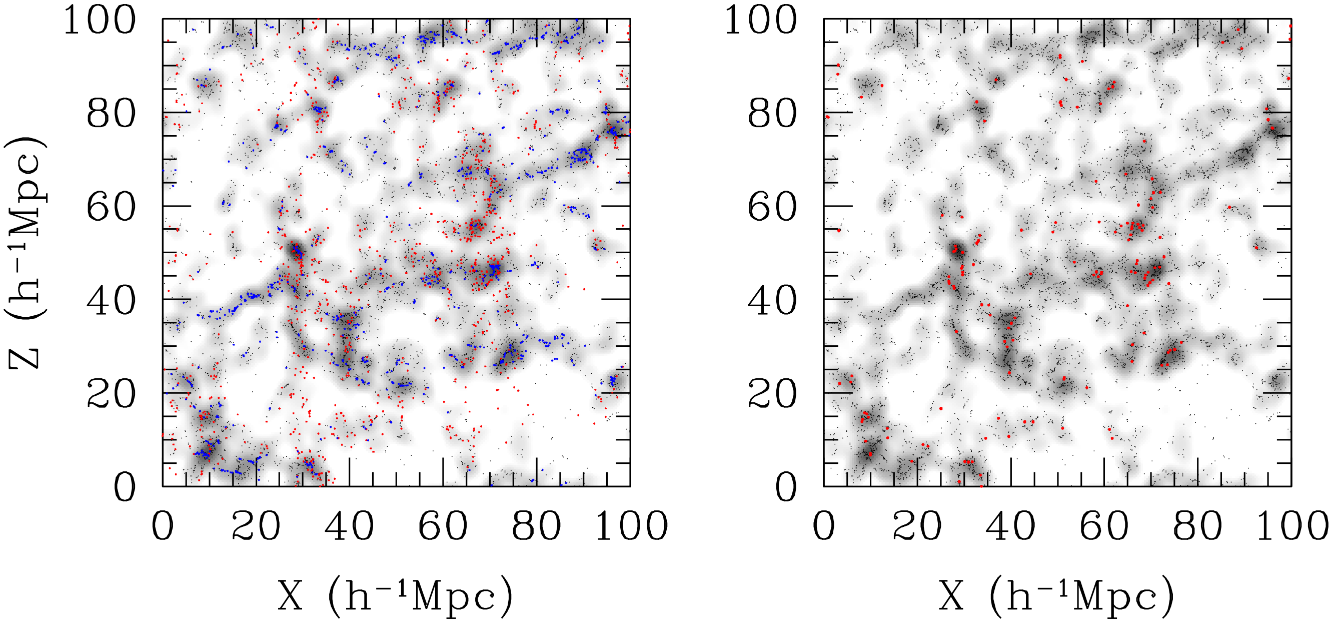

FIG. 4.— Spatial distribution of LAEs. The slice is $5h^{-1}$Mpc thick. The gray scale map shows the matter density distribution (smoothed at $2h^{-1}$Mpc scales; darker for higher density) to delineate the large-scale filamentary structures. Points represent halos above $5\times10^{9}h^{-1}M_{\odot}$. Left: distribution of LAEs as a function of the ratio of the apparent (observed) and intrinsic Lyα luminosity $L_{\rm apparent}/L_{\rm intrinsic}$. Red (blue) points are for sources with Lyα luminosity weakly (strongly) suppressed, with the apparent to intrinsic luminosity ratio higher than 14% (lower than 0.6%), which approximately corresponds to the top (bottom) 10% of the luminosity ratio distribution. Right: distribution of LAEs (red points) above a threshold in apparent (observed) luminosity. The luminosity threshold corresponds to a LAE number density of $3.8\times10^{-3}h^{3}$Mpc^{-3}. Note that the line-of-sight direction (from the observer to sources) is along the $-Z$-direction. That is, the distant observer observes the sources from the top of the panels, which matters for interpreting the relation between Lyα flux suppression and the local environment (see the text).

tribution of LAEs in Figure 4. In our Lyα RT calculation, the observational direction is along the $-Z$-direction, i.e., the observer is assumed to observe from the top of the plot. Points denote all the halos more massive than $9\times10^{9}h^{-1}M_{\odot}$. In the left panel, red points represent sources with weak Lyα flux suppression (high ratio of $L_{\rm apparent}/L_{\rm intrinsic}$) and blue points are for sources with strong Lyα flux suppression (low ratio of $L_{\rm apparent}/L_{\rm intrinsic}$). One can see the environmental dependence in the sense that sources in underdense regions (larger line-of-sight velocity gradient) have a higher probability of being less suppressed in Lyα flux, e.g., sources around the void at $(X,\,Z)=(35,\,20)$. One can also see the line-of-sight density gradient effect. Sources on the near side of an overdense region are more likely to be less suppressed in Lyα flux, e.g., sources above and below the overdense region near $(X,\,Z)=(30,\,40)$.

In the right panel of Figure 4, red points represent LAEs above a threshold in the observed Lyα luminosity. The luminosity threshold corresponds to a sample of LAEs with number density of $3.8\times10^{-3}h^{3}$Mpc^{-3}. The red points therefore show the spatial distributions of observed LAEs. They appear to be strongly clustered with large voids between them. In the next section, we study the clustering of LAEs in more detail.

3. THE CLUSTERING OF LAEs

In this section, we start with the clustering of LAEs in one sample and the associated control samples to show a few new features in galaxy clustering introduced by Lyα RT. Then we present a simple physical model to aid our understanding of these new features. With this model in hand, we study LAE clustering in detail, including the projected/angular clustering and the dependence on observed Lyα luminosity. We present the clustering results from our simulation in terms of the 2PCFs. The fluctuation power spectra for a couple of LAE samples are shown in Appendix B. A comparison between the predictions of LAE clustering in the full Lyα RT and the $\exp(-\tau_\nu)$ models is presented in Appendix C.

3.1. *Real-space and Redshift-space 2PCFs of LAEs*

To mimic observations, we construct LAE samples based on the apparent (*observed*) Lyα luminosity, with each sample consisting of all LAEs with observed Lyα luminosity above a threshold. For such luminosity-threshold samples, luminosity threshold is uniquely mapped onto sample number density. Hereafter, we denote different samples by the number densities of LAEs.

To better illustrate the environment-induced effects, we also construct control samples that are supposed to be free of environment effects induced by Lyα RT. We generate two types of control samples for each LAE sample. The first type is a mass-threshold sample of halos that has the same number density as the LAE sample. This sample corresponds to a model of LAEs that relates observed LAEs to halos through a one-to-one map of observed Lyα luminosity onto halo mass (a.k.a. abundance matching).

The second type of control sample is called the shuffled LAE sample (S-LAEs). The sample is constructed as follows. We first sort halos by mass and divide them into narrow mass bins with typical bin width of 0.02–0.04 dex in $\log M$. The number of halos in each bin is a few thou-

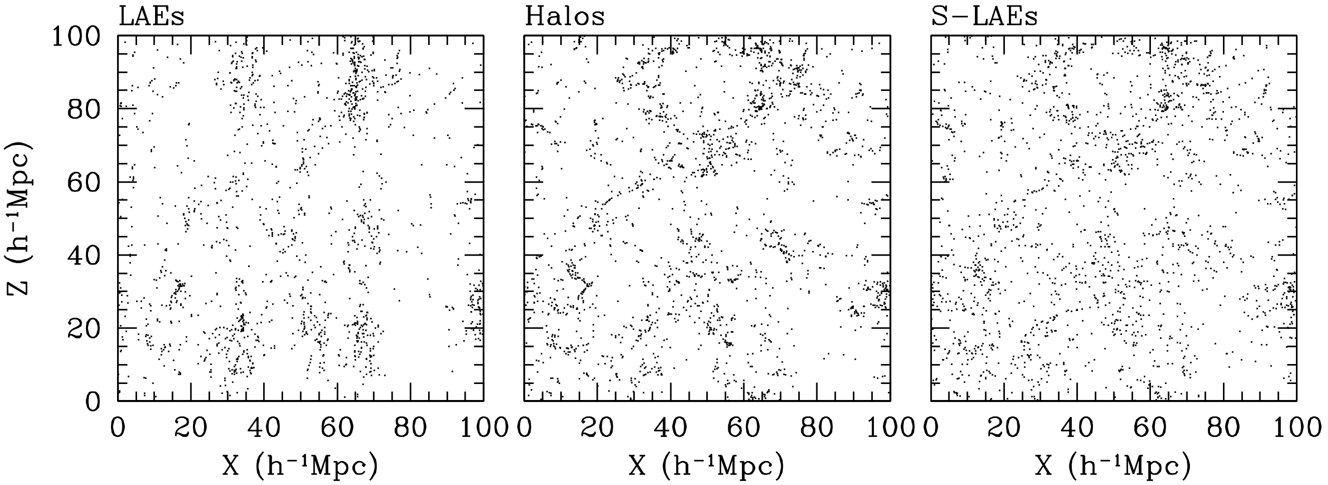

FIG. 5.— Spatial distributions of LAEs and control sources in real space, with one spatial direction being along the line of sight. For LAEs (left panel), the observer is supposed to be on the top of the panel, observing toward the $-Z$-direction. The slice in each panel is from the same part of the box projected onto the X–Z plane, with a thickness of $20h^{-1}$Mpc. The two control samples are the halo sample (middle panel) and the shuffled LAE sample (S-LAEs; right panel), with the same number density ($10^{-2}h^3$Mpc^{-3}) as the LAE sample. The LAE/S-LAE and halo samples are defined by thresholds in observed Lyα luminosity and halo mass, respectively. The shuffled LAE sample is expected to eliminate the effect of environmental dependence of Lyα RT. Compared with the two control samples, the LAE sample shows a prominent pattern of elongated distribution along the line of sight, a result of environment-dependent Lyα RT. See the text for details.

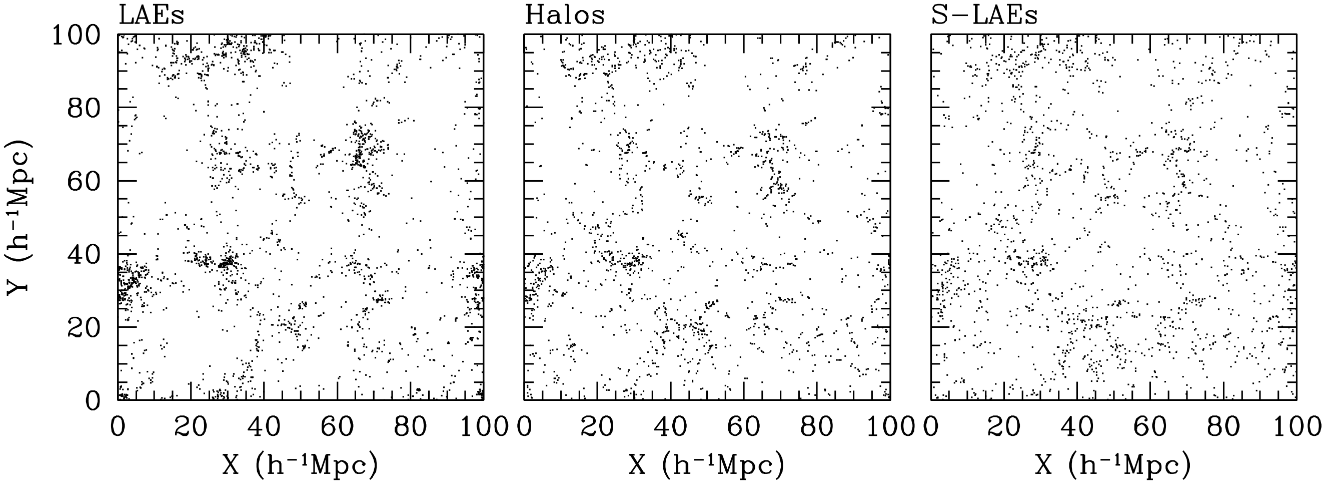

FIG. 6.— Same as Figure 5, but for distributions in the transverse plane perpendicular to the line of sight. In the transverse direction, the LAE sample appears to be more strongly clustered than the two control samples, which is a result of environment-dependent Lyα RT. See the text for details.

sands (hundreds) around $10^{10}h^{-1}M_\odot$ ($10^{11}h^{-1}M_\odot$). For halos in each narrow mass bin, the Lyα emission properties (apparent/intrinsic Lyα luminosity, Lyα spectra, and even the UV luminosity) as a whole are randomly shuffled among them. Such a shuffling algorithm does not lead to any change in the Lyα LF, UV LF, and the relation between observed to intrinsic Lyα properties, which keeps the interpretations to the observed properties of LAEs presented in Paper I unchanged. However, the shuffling is supposed to get rid of any correlation between observed Lyα properties and environments, with the latter encoded in halo positions. From this shuffled catalog, we form the S-LAE sample above the same threshold in observed Lyα luminosity as in the LAE sample. By construction, the S-LAE sample has the same number density as the LAE sample. For the S-LAE sample, the dependence of Lyα RT results on environment is completely eliminated while the statistical properties of Lyα luminosity is kept, making it a more suitable control sample than the halo sample. Similar shuffling method is applied in studying environment effect on halo clustering (assembly bias; e.g., Yoo et al. 2006; Croton et al. 2007; Zu et al. 2008). However, we emphasize that what we intend to study here is not the effect of environments on halo clustering, which is small for galaxy-host halos at high redshifts (e.g., Wechsler et al. 2006; Gao & White 2007), but the effect of the environment-dependent Lyα RT on LAE clustering.

We perform nine realizations of shuffling with different random seeds. For each LAE sample, nine S-LAE sam-

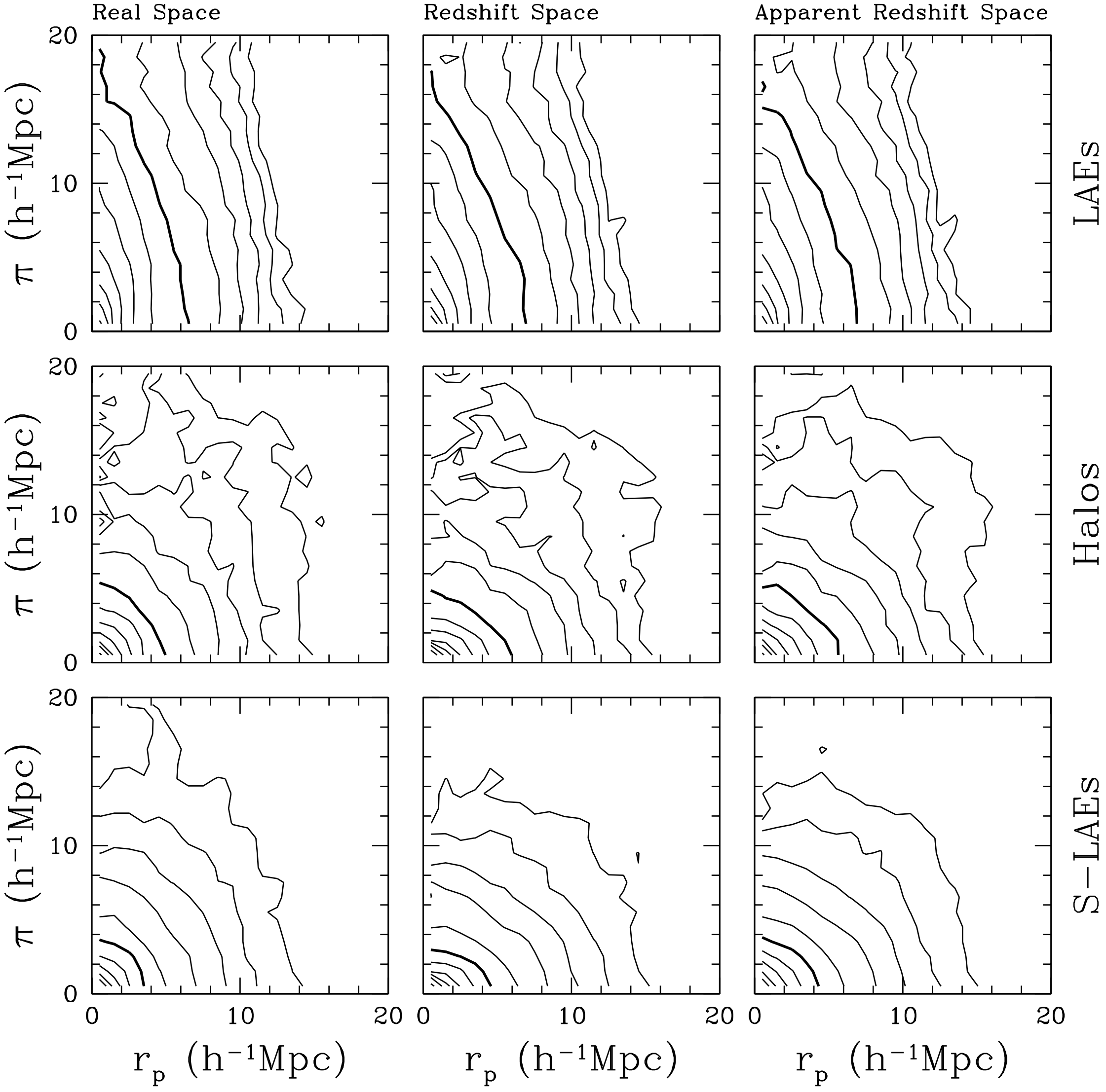

FIG. 7.— Three-dimensional (3D) two-point correlation functions of LAEs and halos as a function of the line-of-sight separation (r_p) and the transverse separation (π). From top to bottom are those of LAEs, halos, and shuffled LAEs (S-LAEs). All samples are threshold samples with the same number density ($10^{-2}h^3\mathrm{Mpc}^{-3}$), with the thresholds being the apparent (observed) Lyα luminosity for LAEs/S-LAEs samples and halo mass for the halo sample, respectively. From left to right are the two-point correlation functions in real space, redshift space, and apparent redshift space. In real space, the position of a source is just its comoving position. In redshift space, the position is determined by the source's comoving position and peculiar velocity. The apparent redshift is defined from the observed peak in Lyα spectra, which has the additional shift caused by Lyα RT (see the text). It is used to determine a source's position in apparent redshift space. The solid contour in each panel denotes a contour level of unity, and the adjacent contours differ by 0.2dex in contour levels. Note the prominent elongation pattern along the line of sight in the clustering of LAEs in all three spaces considered here. See the text.

ples are constructed from these realizations. The statistical results for S-LAEs (e.g., correlation functions) presented in this paper are always the average over the nine realizations.

In Figure 5, the real-space spatial distributions in the X–Z plane of the LAE sample and the two corresponding control samples are compared. All the three samples have number density of $10^{-2}h^3\mathrm{Mpc}^{-3}$. By the term "real space", we mean to use the comoving coordinates of sources, with no peculiar velocity displacements. Each slice has a thickness of $20h^{-1}$Mpc. The line-of-sight direction is along $-Z$. Unlike sources in the control samples, the spatial distribution of LAEs shows a distinct pattern stretching along the line of sight. The elongation resembles the fingers-of-God (FoG) effect seen in redshift-space galaxy clustering. However, it clearly differs from the FoG effect. First, the elongation effect for the LAE sample shows up in real space. Second, while the FoG effect is on scales of virialized halos, the elongation effect for the LAE sample exists up to much larger scales.

For the two control samples, there is no elongation pattern. The clustering of the S-LAE sample appears to be weaker than the halo sample. Although the two samples have the same number density, there are S-LAEs residing in halos of mass lower than the mass threshold of the halo control sample (see Section 4). Since low-mass halos are less clustered than high-mass halos, the S-LAE sample displays a weaker clustering pattern.

In Figure 6, the real-space spatial distributions of sources in the X–Y plane (perpendicular to the line of sight) are compared for the three samples. For the two control samples, the trend is the same as in Figure 5, as expected. The LAE samples show much stronger clustering than the control S-LAE sample. For this particular set of samples, it is also true that LAEs are more strongly clustered than halos in the halo control sample.

The different effects of Lyα selection on the line-of-sight and transverse distributions of LAEs means that the spatial distribution (hence the clustering) of LAEs is no longer isotropic even in real space. We measure the 3D 2PCFs of the LAE and control samples using the Landy–Szalay estimator (Landy & Szalay 1993). The real-space 3D 2PCF $\xi(r_p, \pi)$ for the above LAE sample (top-left panel of Figure 7) clearly shows the anisotropy in LAE clustering, where r_p and π are the transverse and line-of-sight separations of galaxy pairs, respectively. The contours are elongated along the line-of-sight separation. The scales range from sub-Mpc to $> 10h^{-1}$Mpc, where the 2PCF can be accurately measured. The 2PCFs of sources in the halo and S-LAE control samples (middle-left and bottom-left panels) appear to be isotropic, manifested by contours being circular. Note that the deviation from circular contours at large separation for the control samples is caused by statistical fluctuations (sample variance) with the finite simulation box.

In redshift space, there is a well-known effect (Kaiser effect; Kaiser 1987) that introduces anisotropy in galaxy clustering on linear scales, which makes the 2PCF contours squashed along the line of sight. The linear Kaiser effect is clearly seen for the control samples in redshift space (the two lower panels in the middle column of Figure 7). However, for the LAE sample, the prominent elongation pattern along the line of sight is preserved in redshift space, with a slight reduction in the degree of the elongation.

In the above discussion, the redshift-space source positions are calculated as the sum of comoving coordinates and the apparent position change introduced by the line-of-sight peculiar velocity. In practice, if redshifts of LAEs are determined from Lyα line peak in spectra, there would be an additional shift in the apparent position. As shown in Paper I, the observed Lyα line peak generally shifts redward as a consequence of RT and the shift is correlated with the environment. We name the redshift measured from Lyα line peak as apparent redshift and the corresponding redshift space as apparent redshift space. The 2PCFs in the apparent redshift space (right column in Figure 7) look similar to those in the (true) redshift space (middle column in Figure 7). Since at a fixed (true) redshift the apparent redshift has a distribution, the 2PCF contours in apparent redshift space are slightly smoothed. *In all the following discussions, when we refer to redshift-space measurements, we use apparent redshifts for LAE and S-LAE samples and (true) redshifts for halo samples, unless mentioned explicitly.*

We see that our RT model of LAEs predicts that the clustering of observed LAEs differ significantly from those of halos and S-LAEs, which are constructed to be immune to the environment effect on Lyα RT. Before presenting more results in LAE clustering, it is useful to gain some understanding of the basic features in the clustering of LAEs, for which we give an intuitive picture and introduce a simple physical model.

3.2. *Understanding the Clustering of LAEs*

3.2.1. *An Intuitive Picture*

The new features appearing in LAE clustering are related to the selection imposed by Lyα RT, which is closely related to the environment around the LAE sources. Since the main feature in the 2PCF is a line-of-sight distortion, bearing some analogy to redshift-space distortion, we start from an intuitive understanding of LAE clustering by making comparisons to redshift-space distortion.

The effect of redshift-space distortion in the linear regime (Kaiser 1987) is illustrated in Figure 8(a). The solid black curve shows the real-space line-of-sight density distribution of a sample of galaxies, with one mode of the plane-wave fluctuation considered. The arrows indicate peculiar velocities of galaxies with the length representing the amplitude. In general, galaxies fall into overdense regions and stream out of underdense regions. When mapped onto redshift space, the line-of-sight density distribution of galaxies changes because of the additional redshifts caused by peculiar velocities. As a result, in redshift space, overdense regions become more overdense and underdense regions become more underdense, as shown by the red curve. Redshift-space distortion only takes effect along the line of sight, which leads to an enhancement of the line-of-sight fluctuations. In terms of the 3D 2PCF, the effect shows up as contours squashed along the line of sight.

For LAEs, the dependence of Lyα RT on environments leads to a selection function that determines whether a source can be detected as LAEs given the flux limit in observation. Figure 8(b) illustrates such a selection effect. The black curve is the real-space line-of-sight density distribution of an underlying population of LAEs (e.g., all the halos that could be detected as LAEs given the flux limit in observation, if there were no Lyα RT effect). As shown in Section 2, the line-of-sight velocity gradient has the strongest effect in determining the observed-to-intrinsic Lyα luminosity ratio, larger gradient for higher ratio. For the plane-wave fluctuation in Figure 8(b), the velocity gradient reaches its maximum and minimum at the trough of the underdense region and the peak of the overdense region, respectively. As a result, sources in the underdense region have a higher probability to be observed as LAEs than those in the overdense region, making the overdense region less overdense and the underdense region less underdense (i.e., suppressing the line-of-sight fluctuation). The density distribution of LAEs that can be observed is shown as the solid red curve (note that we also add a phase shift to reflect the dependence of the selection on density and velocity gradients). The dotted red line is the mean density of LAEs, and the difference with respect to the dotted black line is an overall selection effect caused by Lyα RT. The illustration shows that the Lyα selection effect is similar to redshift-space distortion, but it originates in real space with an opposite sign.

Figure 9 illustrates how to understand the selection effect from the point view of angular distribution of Lyα emission. In Figure 9(a), the grays cale delineates a

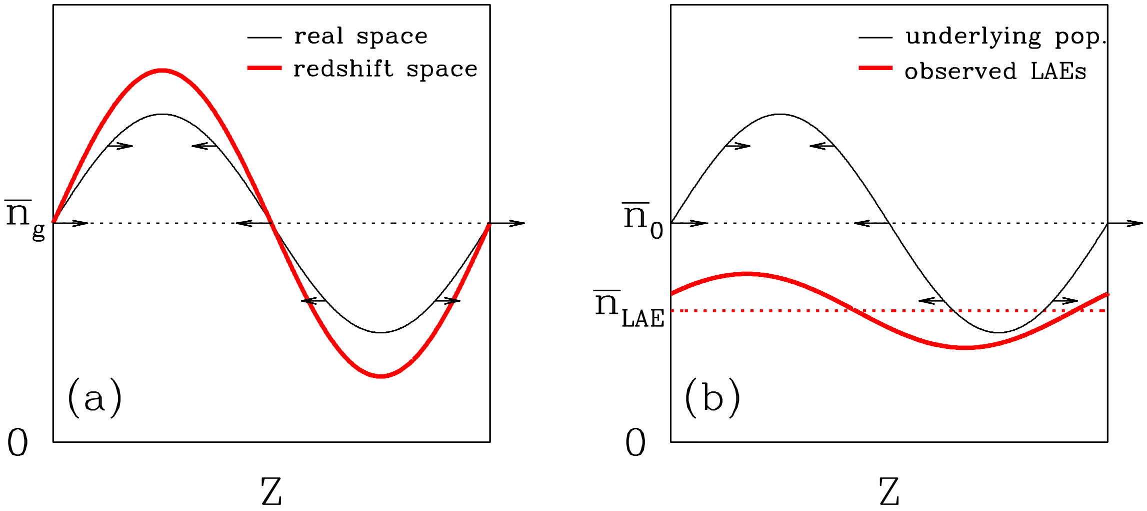

FIG. 8.— Illustration of effects of redshift-space distortion and Lyα RT selection on the observed density fluctuation alone the line of sight. (a): Effect of redshift-space distortion. The solid black/thin curve is the real-space density distribution with the dotted line denoting the mean. Arrows represent the linear peculiar velocity with the length proportional to the amplitude. The red/thick curve represents the density distribution in redshift space. (b): Effect of Lyα RT selection. The solid black/thin curve is the real-space density distribution of a population of galaxies. The observed LAEs are a fraction of these galaxies, with a selection function imposed by the Lyα RT process. The density distribution of the observed LAEs in real-space is represented by the solid red/thick curve. The selection favors sources in regions with low density and positive line-of-sight velocity gradient and to a smaller degree, in regions with receding line-of-sight velocity that are on the near-side (far-side) of overdense (underdense) regions. The observer is assumed to lie on the left side of the panel. See the text for details.

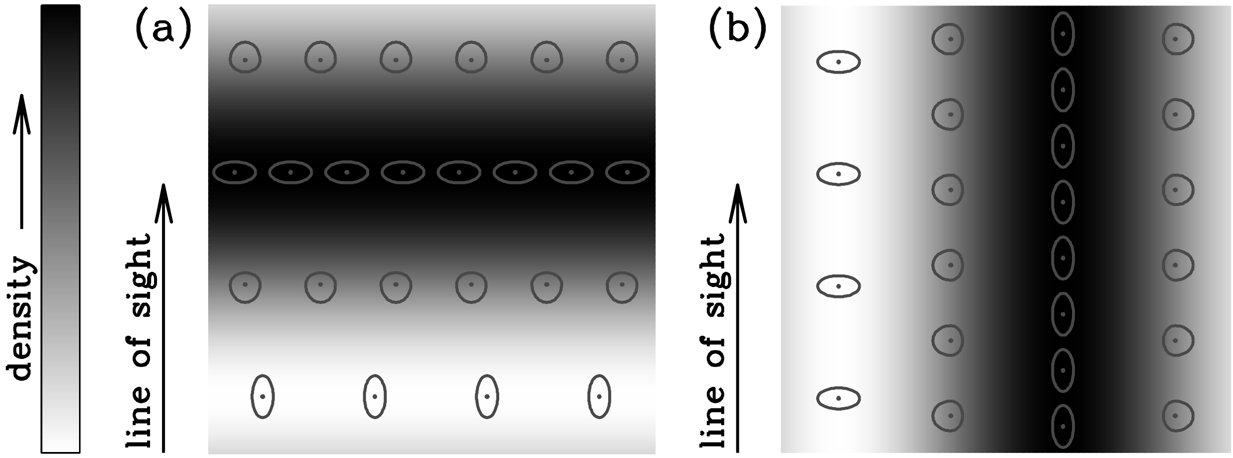

FIG. 9.— Illustration of the Lyα RT selection effect in the cases with fluctuation modes parallel and perpendicular to the line of sight. Panel (a) shows the case of density fluctuation along the line of sight. The gray scale delineates the overdensity across one wavelength of a plane wave, darker for higher overdensity. Each point represents a Lyα emitting source, and the ring around it illustrates the angular distribution of escaped Lyα emission. In the underdense region, Lyα emission preferentially comes out along the line-of-sight direction (and its opposite direction), mainly because of the effect of velocity gradient on the RT (see the text). Sources in the underdense (overdense) region have a higher (lower) probability to be observed than those in the overdense region. Therefore, the Lyα RT selection causes a suppression of the fluctuation along the line of sight. Panel (b) is a 90° rotation of panel (a), corresponding to the case of density fluctuation perpendicular to the line of sight. In this case, the Lyα RT selection causes an enhancement in the fluctuation. See the text for details.

plane-wave density fluctuation along the line of sight, darker for higher density. Each dot is an underlying LAE source. The ring around each source shows the angular distribution of the Lyα emission that can be observed. For example, in the underdense region (white part of the gray scale map), we have a large velocity gradient along the line of sight and zero along the transverse direction. As a consequence, Lyα photons preferentially escape from the directions parallel and anti-parallel to the line of sight, leading to higher surface brightness in these directions. While in the overdense region, the situation changes to the opposite. For an LAE survey set by a Lyα flux limit, sources in the underdense region have a higher probability to be observed as LAEs. Again we reach the same conclusion as above — the line-of-sight density fluctuation is suppressed for LAEs. Note that except for sources residing at the peak and trough of the (plane-wave) density fluctuations, the angular distribution of Lyα emission generally does not have a parity symmetry along the line of sight. For example, Lyα

photons in sources near the boundary between the overdense and underdense regions in Figure 9 have their Lyα photons preferentially escape toward the direction of underdense region, as a result of the density gradient and receding velocity effect.

For the selection effect in the case of a transverse fluctuation, we only need to rotate Figure 9(a) by 90°, which leads to Figure 9(b). In the underdense region, Lyα photons appear to preferentially escape in the direction perpendicular to the line of sight. So sources in the underdense region now have a lower probability to be detected as LAEs. This leads to the interesting result that the density fluctuation in the transverse direction is enhanced for LAEs.

Note that large-scale density filaments are a common feature of gravitational dynamics. Filaments may be described by Figure 9. The net result is that filaments oriented along the line of sight are preferentially observed, whereas those perpendicular to the line of sight are suppressed. This feature is clearly seen in the left panel of Figure 5.

Based on the above discussion, the main selection effects in galaxy clustering caused by environment-dependent Lyα RT can be summarized as the suppression of the fluctuation in the line-of-sight direction and the enhancement of the fluctuation in the transverse direction. In what follows, we present a simple physical model to describe these effects.

3.2.2. *A Simple Physical Model*

For the simple physical model, we limit our discussion to the linear regime. Given that the effects of Lyα selection share some similarities with the Kaiser effect, we first review the formalism of redshift-space distortion in galaxy clustering (see, e.g., Hamilton 1998). We denote quantities in redshift space with a superscript "s".

The linear density fluctuation $\delta_g(\mathbf{r})$ of galaxies in real space may be related to that of matter $\delta_m(\mathbf{r})$ by $\delta_g(\mathbf{r}) = b\delta_m(\mathbf{r})$, where b is the large-scale galaxy bias factor that in general may be scale dependent. From conservation of galaxy pairs, the redshift-space density fluctuation $\delta_g^s(\mathbf{s})$ satisfies

$$[1+\delta_g^s(\mathbf{s})]d^3s = [1+\delta_g(\mathbf{r})]d^3r, \tag{1}$$

with $\mathbf{s} = \mathbf{r} + v_z\hat{z}/(Ha)$, where v_z is the line-of-sight peculiar velocity and H is the Hubble constant at the time when the scale factor is a. Equation (1) reduces to

$$\delta_g^s = \delta_g - \frac{1}{Ha}\frac{\partial v_z}{\partial z}. \tag{2}$$

The relation is easier to study in Fourier space by noticing that $\delta_m = \sum_{\mathbf{k}} \delta_{m,\mathbf{k}} \exp(i\mathbf{k}\cdot\mathbf{r})$ and $\partial v_z/\partial z = -\sum_{\mathbf{k}} fHa(k_z^2/k^2)\delta_{m,\mathbf{k}} \exp(i\mathbf{k}\cdot\mathbf{r})$,

$$\delta_{g,\mathbf{k}}^s = \delta_{g,\mathbf{k}} + f\mu^2\delta_{m,\mathbf{k}} = \left(1+\beta\mu^2\right)\delta_{g,\mathbf{k}}. \tag{3}$$

In the above expression, $\mu = k_z/k$ is the cosine of the angle between the line of sight and the wave vector of the Fourier mode of interest, $f = d\ln G/d\ln a$ is the derivative of the linear growth factor G, and $\beta \equiv f/b$ is the redshift-distortion parameter. The underlying picture of the above equation is that galaxies fall into overdense regions and stream out of underdense regions, enhancing the line-of-sight density fluctuation in redshift space, as illustrated in Figure 8(a). In terms of the power spectrum, we have

$$P_g^s(\mathbf{k}) = (1+\beta\mu^2)^2 P_g(\mathbf{k}). \tag{4}$$

In general, whenever the detection of an object or the measurement of a quantity in redshift space is affected or altered by the gradient of peculiar velocity, there are two different bias factors, one related to density and the other related to peculiar velocity. The β factor in the Kaiser formula may not have its usual meaning. McDonald et al. (2000) and McDonald (2003) discuss this for the case of Lyα forest correlation, where the optical depth or transmitted flux is affected by peculiar velocity gradient. In our case, the selection function of the galaxies varies with the velocity gradient.

For LAEs, the density and line-of-sight peculiar velocity and their line-of-sight gradient, as the primary environmental factors, affect Lyα RT, which imposes a selection function for the appearance of LAEs. For the simple physical model presented here, we only consider the two main factors, line-of-sight peculiar velocity gradient and density. As shown below, including them is able to explain the main effects in LAE clustering. For completeness, in Appendix A, we add the other two factors into the model and show that their main effect is to introduce scale-dependent bias.

We consider a simple case that the selection function is a linear function of the line-of-sight peculiar velocity gradient $\partial v_z/\partial z$ and the matter density δ_m. In this model, the real-space density of LAE galaxies is related to the matter density modified by the selection function,

$$\bar{n}_g(1+\delta_g) = q\bar{n}_0(1+b\delta_m) \times \left[1+\alpha_1\delta_m + \alpha_2\frac{1}{Ha}\frac{\partial v_z}{\partial z}\right], \tag{5}$$

where b is the bias factor for the underlying galaxy population (with mean number density $\bar{n}_0$) before the Lyα selection is imposed, $\bar{n}_g$ is the mean number density of galaxies that are selected as LAEs, q is the overall fraction of galaxies that are selected as LAEs, and α_i (i=1 and 2) are dimensionless coefficients (assumed to be constant). Based on discussions related to Figure 2, the δ_m term in the selection function represents a combined effect of the dependence of Lyα RT on δ_m and the transverse peculiar velocity gradient, and both coefficients α_1 and α_2 are expected to be positive. Although it is more appropriate to separate the terms of density and the transverse peculiar velocity gradient (see Appendix A), we choose to use a positive α_1 to denote the combined effect here for simplicity.

Keeping the first order terms in Equation (5) and noticing that $\bar{n}_g = q\bar{n}_0$, we have

$$\delta_g = (b+\alpha_1)\delta_m + \alpha_2\frac{1}{Ha}\frac{\partial v_z}{\partial z}. \tag{6}$$

In Fourier space, the relation becomes

$$\delta_{g,\mathbf{k}} = \left[(b+\alpha_1) - \alpha_2 f\mu^2\right]\delta_{m,\mathbf{k}}. \tag{7}$$

Since $\partial v_z/\partial z$ is the major variable in shaping the observed-to-intrinsic Lyα luminosity ratio, the coefficient α_2 is expected to be greater than α_1 (also see Figure 2). Equation (7) describes that the effect of Lyα RT selection from the velocity gradient term (α_2 term) is to suppress the fluctuation along the line of sight, as long as $\alpha_2 f$ is not so large to reverse the phase of the fluctuation.

Adding the Kaiser effect to the above Lyα RT selection effect, in redshift space, the relation for the total effect reads

$$\delta^s_{g,\mathbf{k}} = \left[(b+\alpha_1) + (1-\alpha_2)f\mu^2\right]\delta_{m,\mathbf{k}}. \tag{8}$$

With Equation (8), the power spectrum of LAEs in redshift space is then

$$P^s_g(\mathbf{k}) = \left[\left(1+\frac{\alpha_1}{b}\right) + (1-\alpha_2)\beta\mu^2\right]^2 b^2 P_m(\mathbf{k}). \tag{9}$$

This full expression of power spectrum includes both redshift distortion and Lyα selection effects. The usual redshift space linear power spectrum is a special case with the coefficients α_i set to zero. The dependence of Lyα RT on the velocity gradient leads to the same form of angular dependence as the redshift distortion in the anisotropic power spectrum, but with an opposite sign.

The power spectrum in Equation (9) can be decomposed into monopole, quadrupole, and hexadecapole moments,

$$\begin{aligned} P_0(k) = &\left[\left(1+\frac{\alpha_1}{b}\right)^2 + \frac{2}{3}\left(1+\frac{\alpha_1}{b}\right)(1-\alpha_2)\beta\right. \\ &\left. + \frac{1}{5}(1-\alpha_2)^2\beta^2\right] b^2 P_m(k), \end{aligned} \tag{10}$$

$$P_2(k) = \left[\frac{4}{3}\left(1+\frac{\alpha_1}{b}\right)(1-\alpha_2)\beta + \frac{4}{7}(1-\alpha_2)^2\beta^2\right] b^2 P_m(k), \tag{11}$$

and

$$P_4(k) = \frac{8}{35}(1-\alpha_2)^2\beta^2 b^2 P_m(k). \tag{12}$$

The changes in these multipole moments with respect to the redshift-distortion-only case ($\alpha_i = 0$) can be clearly seen. The monopole and quadrupole are affected by both Lyα selection factors, while the hexadecapole only has additional contributions from the dependence on velocity gradient.

The coefficients in Equation (9) represent the magnitude of the Lyα selection effect. As shown in Figure 7, the elongation pattern along the line of sight is clearly seen in redshift space. Since this is mainly caused by the velocity gradient term, it means that $\alpha_2 > 1$. The α_1 term represents the combined effect of density and transverse velocity gradient. We can imagine that there are cases that the dependence on density itself is strong. For example, at the reionization stage when ionizing bubbles do not percolate yet, there are isolated ionized and neutral regions. If the clustering of sources in overdense regions makes these regions ionize earlier, we expect a strong dependence of Lyα observability on density (a large α_1), which would substantially enhance the clustering of LAEs (Equation (9)). We will examine this in more detail in a subsequent investigation of Lyα RT at higher redshifts where the neutral fraction of the IGM is higher and its fluctuation larger.

In practice, it is hard to measure the 3D clustering of LAEs, since it needs a large spectroscopic sample of LAEs. The 2D clustering, in particular the angular 2PCF, is relatively easy to measure with narrow-band surveys. The angular 2PCF is closely related to the projected 2PCF w_p, which is the 3D 2PCF $\xi(r_p, \pi)$ integrated over the line-of-sight separation,

$$w_p(r_p) = \int_{-\infty}^{+\infty} \xi(r_p, \pi) d\pi. \tag{13}$$

The projected 2PCF is the 2D Fourier transform of the power spectrum with the line-of-sight wave vector set to zero (see Equation (4) of Zheng 2004). From equation (9), the projected 2PCF of LAEs corresponds to the following 2D power spectrum

$$P_g(\mathbf{k}_p) = \left(1+\frac{\alpha_1}{b}\right)^2 b^2 P_m(\mathbf{k}_p), \tag{14}$$

where $\mathbf{k}_p$ is the wave vector in the plane perpendicular to the line of sight. Since $\alpha_1 > 0$, Equation (14) means that the transverse fluctuation is enhanced for LAEs, as schematically shown in Figure 9.

This highly simplified model enables us to see how different environment factors related to Lyα selection affect the power spectrum of LAEs. A realistic model is expected to be more complicated. For example, the simple model assumes that the selection function is a linear combination of environment variables. From Figure 1, we see that the selection does not have a simple linear dependence on any of the factors. In fact, the observed-to-intrinsic Lyα luminosity ratio approximately shows an exponential dependence on environmental variables. Furthermore, the selection depends on halo mass. The simple model is nevertheless useful for understanding features in the clustering of LAEs, and it is able to describe the main effects of Lyα selection on LAE clustering. The form of the power spectrum in Equation (9) and in Appendix A may be a starting point for a fitting formula. In what follows we study LAE clustering in more detail and use the simple model to aid our understanding.

3.3. *3D 2PCFs of LAEs*

In this section, we present the 3D 2PCFs for threshold LAE samples. For each LAE sample, we compare the results to those of the two threshold control samples (halos and S-LAEs) of the same number density.

Figure 10 shows the real-space 3D 2PCFs as a function of sample number density. The 2PCFs of all LAE samples clearly show the elongation pattern along the line-of-sight direction, even though that of the $n = 2\times10^{-4}h^3\mathrm{Mpc}^{-3}$ sample is somewhat noisy. The contours of the 2PCFs for the control samples appear to be circular except for the statistical fluctuation at large scales.

In redshift space, the elongation pattern in the 3D 2PCFs of LAEs is still preserved (Figure 11), implying that the Lyα selection effect is much stronger than the redshift-space distortion effect. For control samples, the contours of 2PCFs are still close to circular. Control samples are only affected by the redshift-space distortion effect. Halos or S-LAEs at $z = 5.7$ are highly biased, so the redshift distortion parameter $\beta \approx \Omega_m^{0.6}/b \sim 1/b$ is small (see Equation (4)), which explains the weak redshift distortion seen in the 2PCFs of control samples.

For all the samples considered here, the 3D 2PCFs of LAEs are characterized by elongation contours on scales

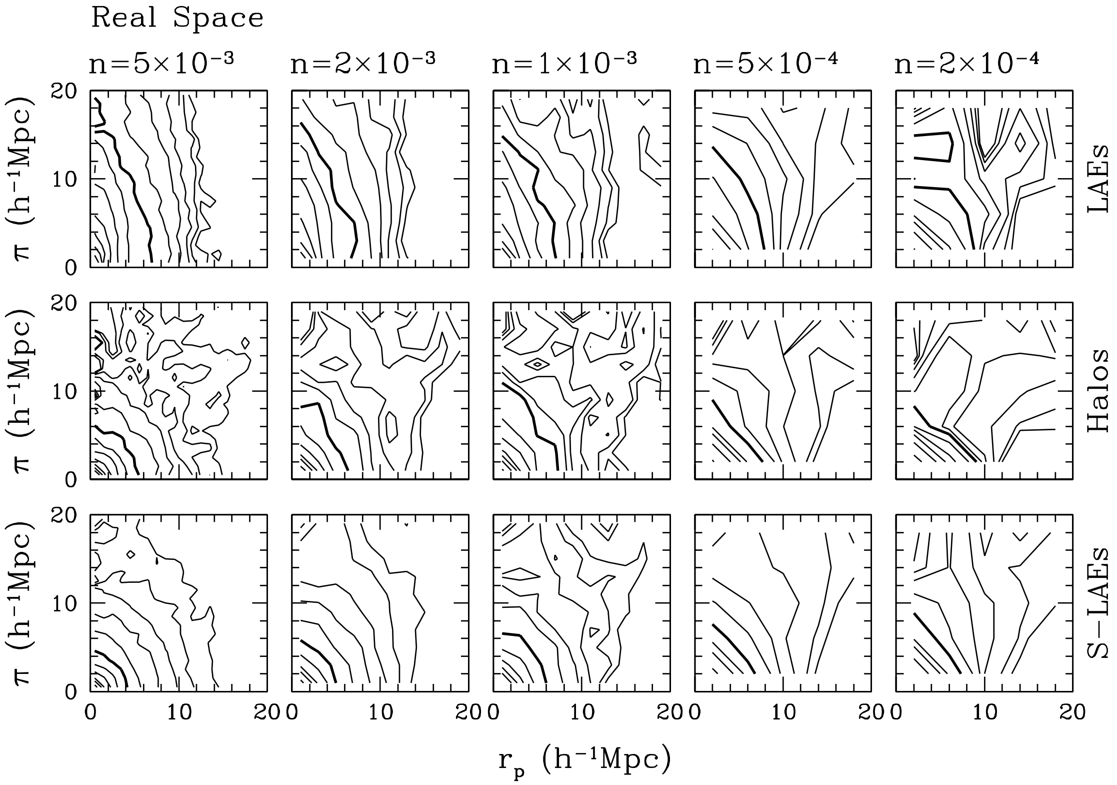

FIG. 10.— Real-space 3D two-point correlation functions $\xi(r_p, \pi)$ for threshold samples. The top column shows the case for LAE samples. For each LAE sample, the middle and bottom columns show the cases for two types of control samples — halos and shuffled LAE samples (S-LAEs), both having the same number density as the corresponding LAE sample. The shuffled LAE sample is expected to eliminate the effect of environmental dependence of Lyα RT (see the text for details). For LAE and S-LAE samples, thresholds in observed Lyα luminosity are used to select sources, while for halos, the thresholds are in halo mass. The number density (in units of $h^3\mathrm{Mpc}^{-3}$) of each set of samples is labeled at the top of each column.

ranging from $\sim$ 1Mpc to a few tens of Mpc, a completely new phenomenon in galaxy clustering predicted by our model. If the anisotropic 3D clustering can be measured from LAE surveys, it will be a direct test of our model and the Lyα RT selection effect. Since the volume of the simulation we use is $10^6h^{-3}\mathrm{Mpc}^3$, Figure 11 implies that a few hundred LAEs with spectroscopic redshifts are needed to have decent measurements of the 3D 2PCFs. Current LAE surveys, such as the LALA survey (Kovač et al. 2007; Wang et al. 2009) and SXDS (Ouchi et al. 2008), are approaching this requirement.

Figures 12 and 13 show the spherically averaged 3D 2PCFs of LAEs and control samples as a function of number density. The error bars are obtained with the jackknife method, whereby we divide the simulation box into eight octants and measure the 2PCFs by excluding one octant at a time. The control samples are halos and S-LAEs in the two figures, respectively. These plots allow a comparison of the overall amplitudes of 2PCFs. In each panel, points are the spherically averaged real-space 3D 2PCFs and curves are averaged from redshift-space 3D 2PCFs. The difference between the real-space and redshift-space average is small, which again demonstrates that the redshift-distortion effect is weak for sources at $z = 5.7$.

The spherically averaged 2PCFs of halos appear to be slightly steeper than those of LAEs (Figure 12). On large scales ($\sim 1 - 10h^{-1}$Mpc), LAEs are more clustered than halos for high number density samples, a consequence of the enhancement of LAE clustering by Lyα selection. At number density $10^{-4}h^3\mathrm{Mpc}^{-3}$, the amplitude of the 2PCF of halos exceeds that of LAEs. The trend of the relative amplitude between LAE and halo samples reflects the competition of the Lyα selection effect and halo bias. At fixed number density, LAEs can populate into halos of mass lower than the mass threshold that defines the halo control sample. One would naively expect that LAEs should be less clustered than halos. However, the selection effect from Lyα RT boosts the clustering of LAEs (Equation (9) and Equation (10)). So we see that LAEs are more clustered than halos for samples with high number density. To explain the relative amplitude at the low number density end, we need to note that halo bias factor is a steeply rising function toward low number density (i.e., toward more massive and rare halos). At very low number density, the boost from Lyα selection in LAE clustering can no longer catch up with the steep increase in halo bias factor, which results in the reversal of the relative 2PCF amplitude.

The S-LAEs, on the other hand, seem to always have a lower amplitude in the spherically averaged 2PCF than the LAEs of the same number density (Figure 13). S-LAE samples are fairer control samples than halo samples, since they share the same statistical properties of Lyα emission with the LAE samples except for the environmental effect on Lyα RT. The LAE and S-LAE samples of the same number density have the same underlying population. Setting the coefficients α_1 and α_2

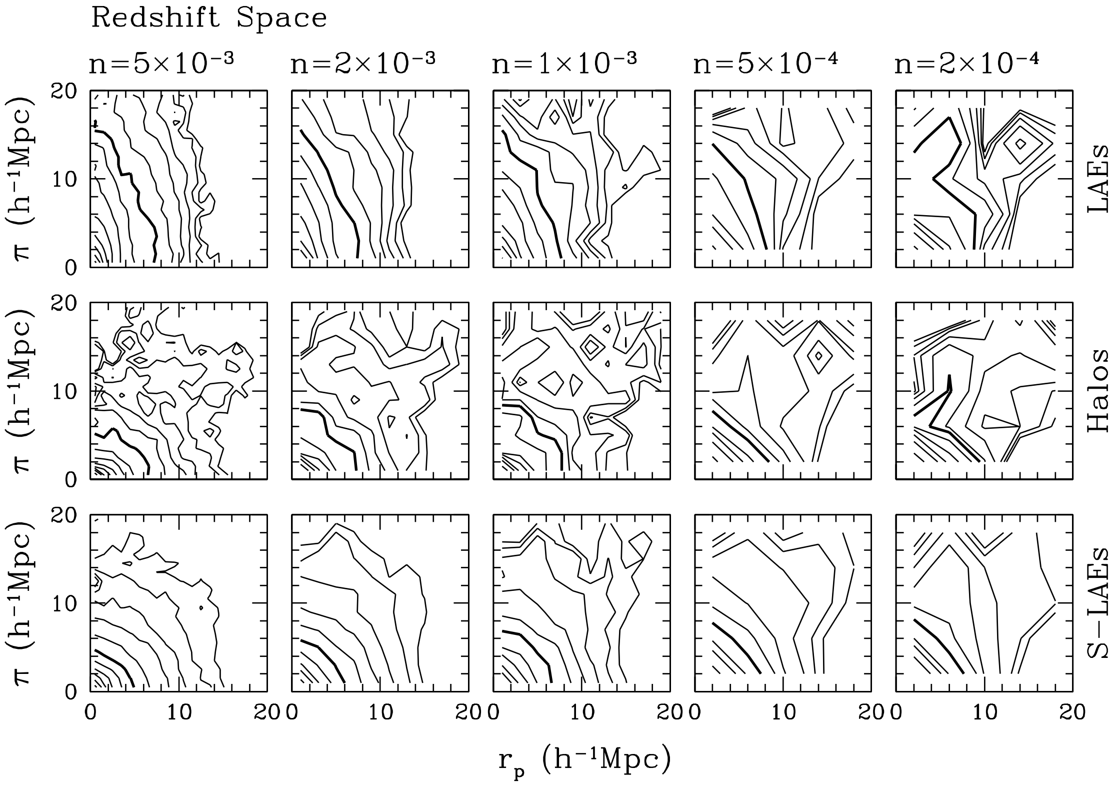

Fig. 11.— Same as in Figure 10, but for redshift-space 3D two-point correlation functions.

to zero in the simple physical model (e.g., Equation (9) and Equation (10)) corresponds to the cases of S-LAEs. From the S-LAE and matter 2PCFs in Figure 13, the bias factor b is of the order of 10, so the redshift distortion parameter β is at the level of 0.1. The monopole of the power spectrum (Equation (10)) is likely to be dominated by the first term, which is from the density dependence. The LAE sample therefore always has enhanced clustering with respect to the corresponding S-LAE sample. As the bias factor b in Equation (10) increases with decreasing sample number density, we expect the enhancement effect to become weaker at lower number density, consistent with what is seen in Figure 13. For $n = 10^{-4}h^3\mathrm{Mpc}^{-3}$, the 2PCFs of the LAE and S-LAE samples are quite close to each other.

3.4. *Projected/Angular 2PCFs of LAEs*

The angular 2PCFs of LAEs can be measured with LAEs identified in narrow-band surveys. On scales smaller than the length scale of the redshift range of the survey, which is set by the width of the narrow-band filter, the angular 2PCF is closely related to the projected 2PCF, or the projected power spectrum (Equation (14)). Here we present the projected 2PCFs of LAE samples and the corresponding control samples in Figure 14 (with the error bars in the LAE sample estimated from the jackknife method).

The Lyα RT effect boosts the transverse density fluctuation, leading to an enhancement in the projected 2PCFs. In the simple physical model, the enhancement comes from the density dependence of the selection function (Equation (14)), which is an effective description of the complicated dependences of RT on density and line-of-sight and transverse velocity gradients (see Appendix A). The trends in the relative amplitudes between the projected 2PCFs of LAEs and halos and between the projected 2PCFs of LAEs and S-LAEs are similar to those seen in the spherically averaged 2PCFs, as shown in Figure 14.

To quantify the amplitude of the projected 2PCFs of LAE and control samples, we compute an average bias factor of LAEs, S-LAEs, and halos for each sample number density. We measure the projected 2PCF of matter from the matter density field in the simulation (dashed curves in Figure 14). The average bias factor of LAEs/S-LAEs/halos is taken to be the square root of the ratio of the projected 2PCFs of LAEs/S-LAEs/halos and matter, averaged over the range of 1–10h^{-1}Mpc. It turns out that the ratio is not constant at the above scales, being smaller toward larger scales. The error bars we assign to the average bias factors largely reflect this scale dependence.

The left panel of Figure 15 shows the bias factors of LAEs, S-LAEs, and halos, as a function of sample number density. Plotted in the right panel are the bias factors of LAEs/S-LAEs relative to halos. At the same number density, S-LAEs can occupy halos with mass lower than the threshold mass of the halo sample, therefore S-LAE samples always show a lower bias factor than halos. The relative bias factor of S-LAEs and halos is roughly a constant (~0.8) for $n = 10^{-2}$–$10^{-3}h^3\mathrm{Mpc}^{-3}$. It decreases toward lower number density and reaches ~0.6 at $n = 10^{-4}h^3\mathrm{Mpc}^{-3}$.

It is interesting that the bias factor for LAE samples does not show strong dependence on sample number density. The value is around 10 for sample number den-

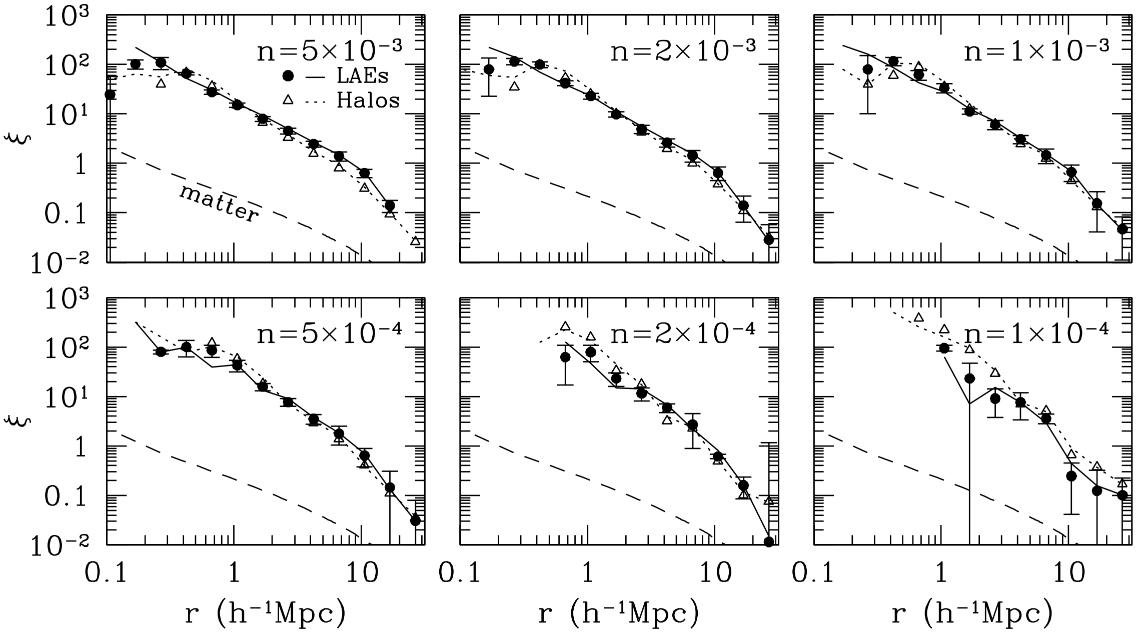

FIG. 12.— Spherically averaged two-point correlation functions of LAEs as a function of number density. In each panel, filled circles are the real space two-point correlation function of LAEs, and open triangles are that for the halo control sample with the same number density. LAE and halo samples are defined by thresholds in observed Lyα luminosity and halo mass, respectively. The number density (in units of h^3Mpc^{-3}) is marked in the panel. The solid and dotted curves are from redshift space for LAEs and halos, respectively. The dashed curve is the two-point correlation function of matter.

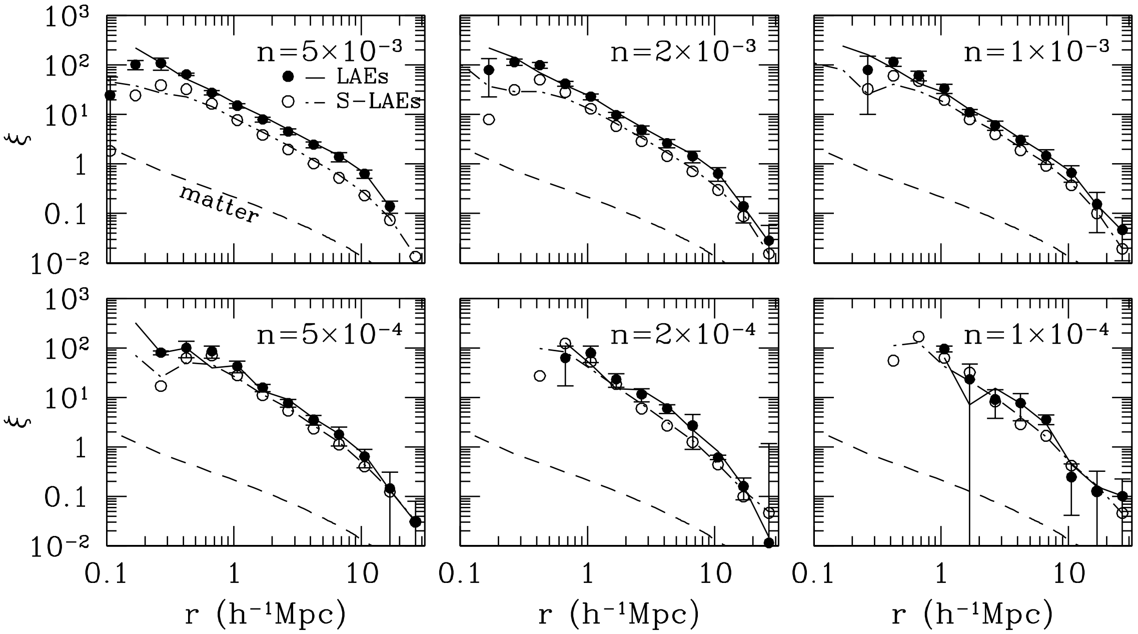

FIG. 13.— Same as Figure 12, with control samples changed to shuffled LAE samples (S-LAEs; open circles and dot-dashed curves). In each panel, LAE and S-LAE sample are defined by the same thresholds in observed Lyα luminosity. Shuffled LAE samples are expected to eliminate the effect of environmental dependence of Lyα RT (see the text for details).

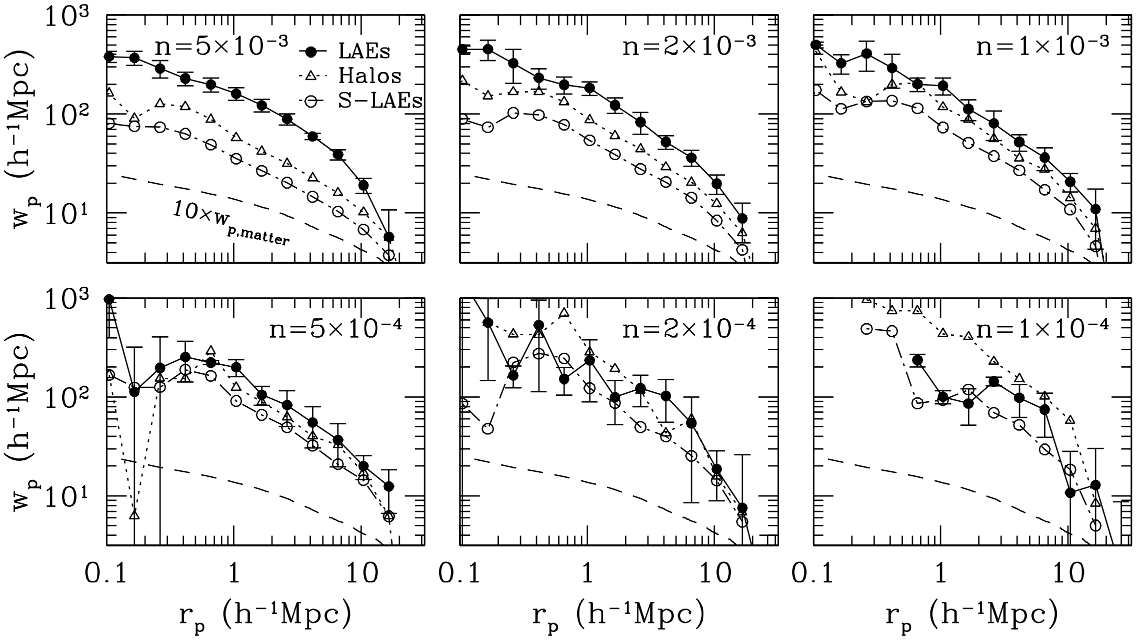

FIG. 14.— Projected two-point correlation functions w_p of LAEs as a function of number density. In each panel, besides the projected two-point correlation function of LAEs (filled circle), we also plot those for the halo control sample (open triangles) and the shuffled LAE sample (S-LAEs; open circles) of the same number density (marked in the panel in units of $h^3\mathrm{Mpc}^{-3}$). LAE/S-LAE and halo samples are defined by thresholds in observed Lyα luminosity and halo mass, respectively. The dashed curve is the projected two-point correlation function of matter, scaled by a factor of 10.

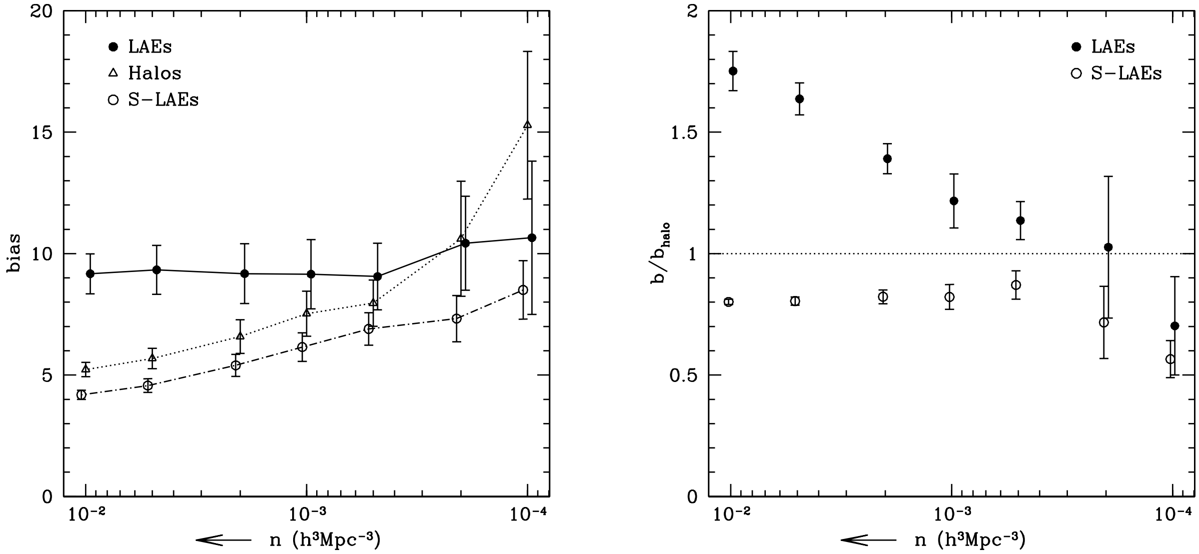

FIG. 15.— Bias factors of LAEs, shuffled LAEs (S-LAEs), and halos as a function of sample number density. Left: absolute bias factor. Right: bias factor relative to halos. The relative bias factor is calculated as the square root of the ratio of the projected two-point correlation functions w_p in Figure 14 of LAEs/S-LAEs and halos, averaged over the range of 1–10h^{-1}Mpc. The absolute bias factor is similarly calculated by using the projected matter 2PCF in Figure 14. For clarity, the points for bias factors of LAEs and S-LAEs are slightly shifted horizontally.

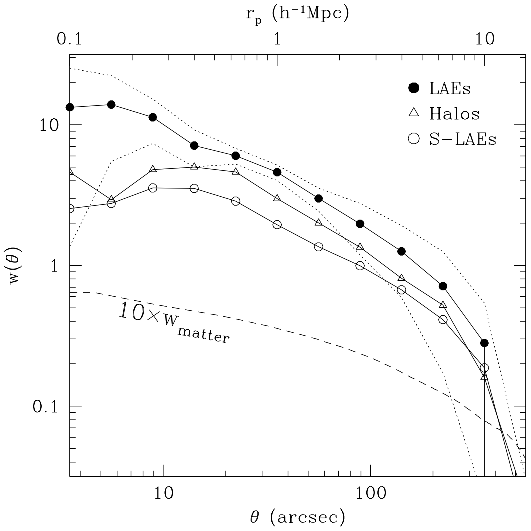

FIG. 16.— Prediction of the angular two-point correlation function for the z ∼5.7 LAE sample in Ouchi et al. (2008). The threshold sample has a number density of $1.2 \times 10^{-3} h^3 \mathrm{Mpc}^{-3}$. The predicted angular two-point correlation function of this sample of LAEs is shown as filled circles. The two dotted curves represent the 1σ scatter expected in a survey with SXDS-like volume. Triangles and open circles are the two-point correlation functions of halos and shuffled LAEs with the same number density as the LAE sample. The dashed curve is the matter correlation function, scaled by a factor of 10.

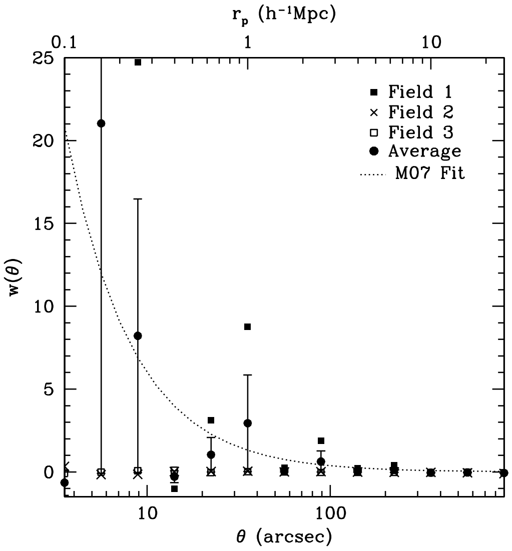

FIG. 17.— Sample variance of the angular two-point correlation function for z ∼5.7 LAE sample in SXDS-like volume. The sample has a number density of $\sim 2 \times 10^{-4} h^3 \mathrm{Mpc}^{-3}$, comparable to the sample in Murayama et al. (2007). Filled squares, crosses, and open squares are the angular two-point correlation functions measured in three fields from the simulation, showing a large sample variance. Filled circles with error bars are the mean of the three measurements. The dotted curve is the best-fit power law to the measured LAE two-point correlation function in Murayama et al. (2007).

sity in the range of 10^{-4}–$10^{-2} h^3 \mathrm{Mpc}^{-3}$ and increases slightly toward the low number density end. However, the bias of LAEs relative to halos continuously decreases toward low number density (filled circles in the right panel), from ∼1.75 at $n = 10^{-2} h^3 \mathrm{Mpc}^{-3}$ to ∼0.7 at $n = 10^{-4} h^3 \mathrm{Mpc}^{-3}$.

The weak dependence of LAE clustering on sample number density is a result of the selection effect caused by the environment dependent Lyα RT. In the simple physical model, the amplitude of the projected 2PCF is proportional to $(b+\alpha_1)^2$ (Equation (14)). As the number density decreases, the bias factor b increases. The weak dependence of the amplitude on number density would require that α_1 drop with decreasing number density, which seems to be consistent with the halo mass dependence seen in Figure 1. The prediction can be tested with LAE clustering measurements as a function of observed Lyα luminosity. In Appendix D, we show how the weak dependence changes if there is a large dispersion in the intrinsic Lyα luminosity and halo mass relation.

When interpreting observational results of galaxy clustering, luminosity-threshold samples of galaxies are usually modeled as mass-threshold halo samples for a simple inference of the relation between galaxies and halos. If the same exercise were applied to Lyα-luminosity-threshold samples of LAEs, our model would have interesting implications. For high number density samples ($n > 5 \times 10^{-4} h^3 \mathrm{Mpc}^{-3}$), LAEs are more strongly clustered than halos in the corresponding mass-threshold halo control sample. From the clustering amplitude, one would relate the LAE sample to a halo sample with higher mass threshold. However, the number density of these halos are less than the LAE sample, which would imply that there have to be multiple LAEs per halo. For example, the bias factor of $n = 2 \times 10^{-3} h^3 \mathrm{Mpc}^{-3}$ LAEs is similar to that of $n = 4 \times 10^{-4} h^3 \mathrm{Mpc}^{-3}$ halos (left panel of Figure 15). From the clustering amplitude, we would infer that these LAEs reside in halos above $2 \times 10^{11} h^{-1} M_\odot$ ($n = 4 \times 10^{-4} h^3 \mathrm{Mpc}^{-3}$), and comparison of the halo number density and LAE number density would make us infer that there are on average five LAEs per halo. If one LAE per halo were assumed, from the number density alone, we would infer that these LAEs reside in halos above $7 \times 10^{10} h^{-1} M_\odot$. For low number density samples ($n < 5 \times 10^{-4} h^3 \mathrm{Mpc}^{-3}$), LAEs are less clustered than halo samples, and one would infer a duty cycle of LAEs by combining the clustering result and the number density. We see that the simple modeling of LAEs as mass-threshold halo samples can lead to incorrect inference of the relation between LAEs and halos. Therefore, a proper interpretation of LAE clustering requires a careful account of the large Lyα selection effect.

At present, the largest LAE sample at $z = 5.7$ comes from the SXDS (Ouchi et al. 2008). If we divided the simulation box along our chosen line of sight into three layers of equal size, the depth of each layer, $33.33 h^{-1}$Mpc, is close to that from the width of the narrow-band filter used to search for z ∼5.7 LAEs in the SXDS, and the area is almost identical to that of the survey (1deg^2). Therefore, the simulation box gives us three SXDS-like volumes at z ∼5.7.

The photometric z ∼5.7 LAE sample in Ouchi et al. (2008) corresponds to a luminosity-threshold sample of number density $1.2 \times 10^{-3} h^3 \mathrm{Mpc}^{-3}$. We construct a threshold sample of model LAEs that has the same number density and use the Landy–Szalay estimator (Landy & Szalay 1993) to measure the angular 2PCFs in the three SXDS-like volumes, respectively. We also perform similar measurements for the halo and S-LAE control samples. In Figure 16, points connected by solid curves are the 2PCFs of LAEs, halos, and S-LAEs, respectively, averaged over the three SXDS-like volumes. Similar to the projected 2PCFs, LAEs and S-LAEs have the highest and lowest angular clustering amplitudes, respectively. The two dotted curves show the variance of the angular 2PCFs of LAEs from individual measurements in the three volumes. Even with the large variance on large scales, the SXDS clustering measurement is likely to reveal that LAEs are more strongly clustered than halos of the same number density.[7]

Murayama et al. (2007) present an angular 2PCF measurement of $z = 5.7$ LAEs in the Cosmic Evolution Survey (COSMOS). The sample number density is about $2 \times 10^{-4} h^3 \mathrm{Mpc}^{-3}$ and the effective area for the sample is 1.86deg^2. They find signals at several scales, but with low significance. The clustering results for this sample in our model are shown in Figure 17. Apparently there is a large variance among samples in the three volumes. The power-law fit from Murayama et al. (2007) (dotted curve) falls in between the three measurements. The Murayama et al. (2007) sample is only 1.86 times larger in effective area than our sample, so we still expect a large sample variance. Large sample variance for low density samples in a small-area survey are reported by Shimasaku et al. (2004) at $z \sim 5$. They measure angular 2PCFs of LAEs at $z = 4.79$ and $z = 4.86$ in a Subaru Deep Field of ∼0.3deg^2 and find clustering signals in one sample and the lack of clustering in the other. Based on the mean and uncertainty from our simulation data for the $2 \times 10^{-4} h^3 \mathrm{Mpc}^{-3}$ sample, we estimate that a survey about 10 times larger is required for a solid detection ($> 3\sigma$) of the clustering signal, which means a ∼10 deg^2 survey. For the (relatively small) scales considered here ($r_p \lesssim 20 h^{-1}$Mpc or $\theta \lesssim 0.2$deg), the survey can be composed of either several separated fields with a few square degrees each or one single contiguous field. With the same total area, the former case would have a slightly smaller number of LAE pairs on the above scales because of the edge effect, so a single field is slightly preferred. The upcoming Subaru Hyper Suprime-Cam (HSC) survey will meet such a requirement.

Based on the above investigation, we conclude that: in the SXDS-like field, large sample variance in angular 2PCFs is expected for LAE samples with low number density (e.g., lower than a few times $10^{-4} h^3 \mathrm{Mpc}^{-3}$); for the LAE sample in Ouchi et al. (2008), it is likely that the enhancement in the transverse clustering of LAEs caused by the Lyα selection effect can be detected. If future observation did not detect this effect and the null detection could be firmly established, it would have profound implications in our understanding of LAEs. It would mean that much stronger effects mask the Lyα RT selection effect, which could be extremely large scatter in the distribution of intrinsic Lyα properties caused by stochastic star formation and/or dust (see further discussions in Section 5 and Appendix D).

4. HOD OF LAEs AND THE ENVIRONMENT DEPENDENCE

The HOD framework (e.g., Berlind & Weinberg 2002) has become a powerful tool to interpret galaxy clustering. It describes the probability distribution of number of galaxies of a given type in a halo as a function of halo mass, together with the spatial and velocity distributions of galaxies inside halos. The HOD framework recasts galaxy clustering in terms of the relation between galaxies and dark matter halos. The link from galaxies to dark matter halos enables informative tests of galaxy formation model and tight constraints on cosmological parameters from galaxy clustering.

The basic assumption in the current version of the HOD framework is that the statistical properties of galaxies only depend on halo mass and is independent of the large-scale environments. For normal galaxies (i.e., galaxies selected from continuum or optically-thin lines), the assumption of environment-independent HOD is supported by theory (e.g., Berlind & Weinberg 2002; but see Zhu et al. 2006), observation (e.g., Blanton et al. 2006), and clustering analysis (e.g., Tinker et al. 2008). Together with the properties of halo population of a given cosmology, the halo-mass-dependent HOD can lead to a full description of galaxy clustering. However, LAEs that are selected from Lyα emission suffer from environment-dependent Lyα RT effect, so the assumption of environment-independent HOD is expected to break down for LAEs.

Figure 18 shows the environment dependence of the HOD of LAEs. Since the line-of-sight velocity gradient is the dominant variable in determining the observed-to-intrinsic Lyα luminosity ratio, we use it to define the environment for the HOD investigation. In each panel, the dashed curve (step function) represents the case for the halo control sample. The mass threshold can be read off from the plot. The solid curve is the mean occupation function of LAEs, averaged over all environments. It is also the mean occupation function of S-LAEs.

In our model, LAEs are related to halos, not sub-halos, and there is one Lyα emitting source per halo, which means that we do not have satellite LAEs. This is a good approximation, since there are few group-size halos at $z = 5.7$. The mass of the most massive halo in the simulation box is $\sim 4 \times 10^{12} h^{-1} M_\odot$, with a virial radius of $\sim 0.4 h^{-1}$Mpc. Ignoring the (low) satellite fraction of LAEs only affects the clustering on small scales (e.g., tenths of Mpc). The mean occupation functions of LAEs in Figure 18 are only for central LAEs and reach unity at the high-mass end.

As mentioned in Paper I, in our LAE model, the intrinsic Lyα luminosity is proportional to halo mass (Equations (1) and (2) in Paper I). If LAEs were selected based on intrinsic Lyα luminosity, they would be equivalent to the halo sample. Observationally, LAEs are selected based on their apparent (observed) Lyα luminosity. We show in Paper I that the environment-dependent Lyα RT leads to a broad distribution of apparent Lyα luminosity at a fixed intrinsic Lyα luminosity. Observation detects LAEs with observed Lyα luminosity above a threshold. This means that for sources at a fixed intrinsic Lyα luminosity (or halo mass), only a fraction of them can be

---

[7] Ouchi et al. (2010) present the angular 2PCF of the $z \sim 5.7$ LAE sample. On scales above $100''$, the measurement agrees with our prediction. However, below $100''$, the measured 2PCF is essentially flattened, which is not seen in their samples at lower and higher redshifts. It may be caused by sample variance or may have interesting implications, which merits further investigations.

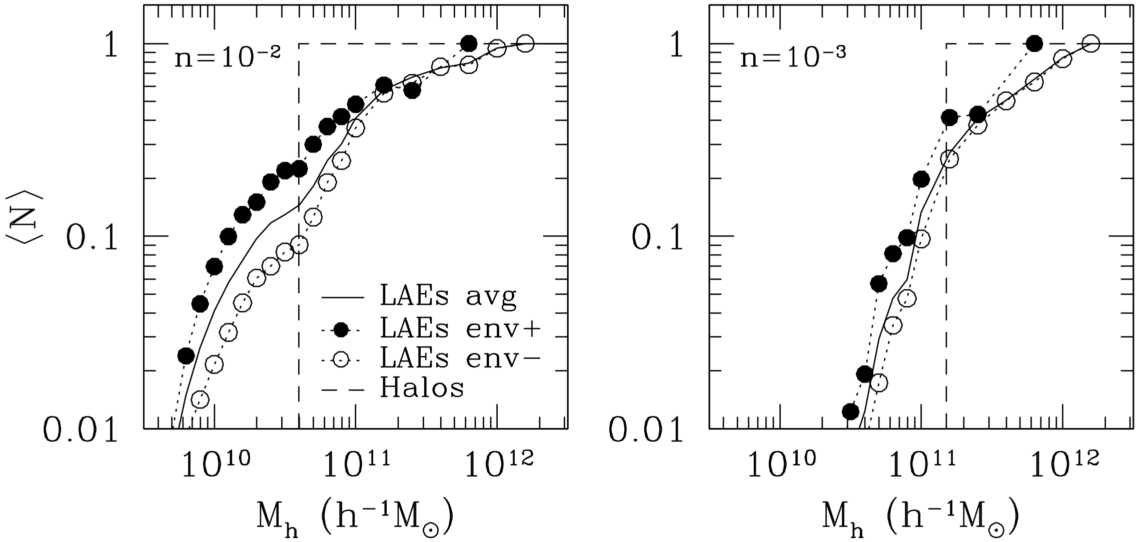

FIG. 18.— Environment dependence of the halo occupation distribution of LAEs. LAE samples are defined by thresholds in observed Lyα luminosity. The left and right panels are for LAE samples with number density of 10^{-2} and $10^{-3}h^3\mathrm{Mpc}^{-3}$, respectively. The line-of-sight velocity gradient $\partial v_z/\partial z$ is used here as the environment indicator and halos are grouped according to the value of $\partial v_z/\partial z$. In each panel, filled (open) circles show the mean occupation function of LAEs in halos that are in the upper (lower) quartile of the $\partial v_z/\partial z$ distribution. The solid curve is the mean occupation function of LAEs over all environments. The dashed curve is the mean occupation function of a threshold halo sample with the same number density.

detected as LAEs. The mean occupation function is simply this fraction. From low to high halo mass, the mean occupation function appears as a ramp from zero to unity (solid curves in Figure 18). With the occupation number below unity, to maintain the same number density as the control halo sample, a fraction of LAEs resides in halos of mass lower than the threshold mass of the halo sample. The cutoff profile of the LAE mean occupation function is similar to that of a luminosity threshold sample of continuum-selected galaxies (e.g., Zheng et al. 2005; Zheng, Coil, & Zehavi 2007), although the profile for LAEs are much more shallow. The shallow cutoffs for LAEs and for continuum-selected galaxies can be attributed to the same origin: for continuum-selected galaxies, the shallow cutoff reflects the scatter in galaxy luminosity at a fixed halo mass, while for LAEs the apparent Lyα luminosity has a distribution at fixed halo mass.

The environment dependence of the HOD of LAEs is demonstrated by the filled and open circles in Figure 18. The filled (open) circles are the mean occupation function of LAEs in halos in the upper (lower) quartile of the $\partial v_z/\partial z$ distribution. Since the observed-to-intrinsic Lyα luminosity ratio is positively correlated with the velocity gradient $\partial v_z/\partial z$, a higher fraction of LAEs in halos with higher $\partial v_z/\partial z$ can be detected, which leads to a higher mean occupation function of LAEs (filled circles) in these halos. The difference between the mean occupation numbers in the upper and lower quartiles of halos are about a factor of 2–3 for the two samples in Figure 18.

If large-scale overdensity δ is added as another environment variable, halos can be grouped according to the joint distribution of $\partial v_z/\partial z$ and δ (Figure 2). We consider two extreme environments. We divide halos in the upper quartile of $\partial v_z/\partial z$ according to the value of δ and keep halos in the upper quartile of δ as the first group. We then divide halos in the lower quartile of $\partial v_z/\partial z$ according to the value of δ and keep halos in the lower quartile of δ as the second group. The two groups of halos correspond to the upper-right and lower-left corners of the shaded region in Figure 2. As the mean observed-to-intrinsic Lyα luminosity ratios for halos in these two groups differ a lot, so does the mean occupation functions of LAEs in the two group of halos. We find that the mean occupation numbers can differ by more than one order of magnitude.

The strong environment dependence of the HOD of LAEs adds complexity to the modeling of their clustering. In fact, from the difference in the clustering of the LAE sample and the halo control sample, we know that the simple model of one LAE per halo with a mass threshold does not work. The difference in the LAE and S-LAE clustering means that the environment-independent HOD model is not a good model, either. To fully describe the features in the LAE clustering, the environment dependence has to be incorporated into the HOD model.

5. CONCLUSION AND DISCUSSION

We investigate the clustering of LAEs, galaxies that are selected by their Lyα emission, within a physical model that fully accounts for the Lyα RT. Our model of LAEs combines radiation-hydrodynamic cosmological reionization simulations with Monte Carlo RT for Lyα photons. It is a simple model, which assumes that RT is the single factor in transforming intrinsic Lyα emission properties to observed ones. As previously shown in Paper I, the simple model is able to explain an array of observational properties of $z = 5.7$ LAEs. The model has strong predictive power, and we predict the clustering properties of LAE clustering in this paper.

Lyα RT depends on the circum-galactic and intergalactic environments of Lyα emitting galaxies. Lyα photons emitted from a source at a halo center see a complex density and velocity structure and an anisotropic optical depth distribution. Lyα photons tend to find the easiest way out, and the observed Lyα emission is usually anisotropic. *We emphasize that the observed Lyα flux at a given line of sight is not purely determined by the line-of-sight optical depth, but the line-of-sight optical depth relative to those in all other directions (see Section 2).* Because of the resonance nature of the Lyα line and the large scattering cross-section, the observed Lyα emission is highly sensitive to the local environments, including the matter density, line-of-sight velocity, their line-of-sight gradients, and the velocity gradients in the transverse directions (not all of these environmental variables are independent). It is this strong coupling between observed Lyα emission and environments that gives rise to new effects in LAE clustering that need to be taken into account in interpreting the clustering of observed LAE samples.

The overall effects in clustering caused by the Lyα selection are anisotropic clustering and scale-dependent galaxy bias. For density fluctuations along the line of sight, Lyα selection leads to a higher probability in detecting LAE sources in underdense regions than in overdense regions, so it suppresses the line-of-sight density fluctuations. For density fluctuations perpendicular to the line of sight, the anisotropic distribution of Lyα emission makes sources in overdense regions preferentially selected, hence the transverse density fluctuations are enhanced. Roughly speaking, filamentary or planar structures tend to be preferentially selected when they are parallel to the line of sight.

The suppression of line-of-sight fluctuations and the enhancement of transverse fluctuations create anisotropy in LAE clustering. The iso-contour curves in the 3D 2PCFs, which reflect LAE pair counts as a function of line-of-sight and transverse separations, show a distinct elongation pattern along the line of sight. The elongation appears on all scales where we have reliable measurements of the 2PCFs, ranging from sub-Mpc to over 10 Mpc. The anisotropic pattern is opposite to the linear redshift-space distortion effect (Kaiser effect), which makes contours squashed along the line of sight. We emphasize that the anisotropy caused by Lyα selection originates in real space. At $z = 5.7$, the cases we consider in this paper, the Lyα-selection-induced distortion in LAE clustering is much stronger than the linear redshift-space distortion. Therefore, even in redshift space the elongation pattern along the line of sight in the 3D 2PCFs is well preserved. We note that the elongation also differs from the FoG effect seen in galaxy clustering, which is caused by random motions of galaxies in virialized structures. While the FoG effect only shows up in redshift space and on small scales (e.g., $\lesssim$ 1Mpc), the Lyα selection effect can appear in both real and redshift spaces and on much larger scales. The Lyα RT induced features are not "Fingers of God" but "Arms of God".

The anisotropic clustering induced by Lyα selection is a completely new phenomenon in galaxy clustering. Other than the usual redshift-space distortion (FoG and Kaiser effect), there are other forms of anisotropic clustering discussed in the literature. Padilla et al. (2005) study the cross-correlation between voids and galaxies. In the redshift-space two-point cross-correlation function of voids and galaxies, an elongation pattern along the line of sight is found on large scales (up to a few times the radius of voids in the sample). Unlike the Lyα selection effect, which is a real-space effect, the phenomenon in the void-galaxy cross-correlation is a redshift-space effect. It simply reflects that galaxies tend to stream out of void regions. The closest analogy to the Lyα selection effect we study is the effect of orientation-dependent galaxy selection investigated by Hirata (2009), in the case that galaxies are aligned by large scale tidal fields. Both effects can be attributed to an environment-dependent surface brightness selection and act in both real and redshift spaces. However, the Lyα RT selection effect is much stronger. While the Hirata effect may change the clustering at a level of a few percent, the Lyα selection can change the clustering amplitude by a factor of a few, owing to the high sensitivity of Lyα RT to local environments of galaxies. In addition, unlike the surface brightness distribution of stars in galaxies, which largely has a parity symmetry (i.e., similar surface brightness if viewed at opposite directions), the anisotropic distribution of Lyα surface brightness does not necessarily have any symmetry.

The 3D anisotropic clustering of LAEs, if measured, will be a strong test to the RT model of LAEs. To achieve this goal, a large spectroscopic sample of LAEs will be needed. With current narrow-band surveys of LAEs, however, the clustering measurements are limited to the angular 2PCFs, which resemble the projected 2PCFs. Unlike the redshift-space distortion effect, which is largely eliminated in the projected 2PCFs, we find that the Lyα selection effect is imprinted in the projected 2PCFs. Projection keeps the transverse fluctuations, which are always enhanced by the Lyα selection. The projected 2PCF of LAEs has a higher amplitude than that of the control LAE sample with environment effect removed. Our model makes the following distinctive prediction (see Figure 15): *the amplitude of the LAE 2PCF has a very weak dependence on the observed Lyα luminosity.* The prediction breaks down for faint LAEs if a large dispersion (1 dex) between intrinsic Lyα luminosity and halo mass is introduced, which may result from stochastic star formation, but it remains valid for luminous LAEs (see Appendix D). This is testable with large narrow-band surveys. The relation between LAEs and underlying halos has interesting properties. For LAE samples defined by a threshold in observed Lyα luminosity, faint LAEs appear to be more strongly clustered than mass threshold samples of dark matter halos having the same number density. The trend is reversed for very bright LAEs (with number density lower than $2 \times 10^{-4} h^3 \mathrm{Mpc}^{-3}$), where halos are more strongly clustered than LAEs of the same number density. If an LAE sample with low luminosity threshold were simply related to a mass threshold sample of halos and one used the observed LAE clustering amplitude to infer the halo number density, one would reach the conclusion that there are multiple LAEs per halo. This is not clearly seen from currently available clustering measurements yet, probably because of the small sample sizes (hence large variance) and the existence of contamination from low-redshift objects.

The Lyα-selection-induced anisotropic clustering can be largely understood by accounting for the dependences of the selection on density and line-of-sight velocity gradient. Besides these dependences, Lyα selection is also related to line-of-sight peculiar velocity and line-of-sight density gradient, which can give rise to scale-dependent galaxy bias, changing the shape of the fluctuation power spectrum with respect to matter (Appendices A and B). We develop a simple physical model that incorporates all the identified environment variables in the selection to aid the understanding and interpretation of LAE clustering (Appendix A). Although the model is able to provide qualitative explanations to features in the LAE clustering, it is an over-simplified model, which assumes linear dependence on environment variables. A more sophisticated model will have to rely on a detailed study of the dependence of Lyα RT on environments and an accurate description of the statistical relation between observed Lyα emission and environmental variables.

As a powerful tool, the HOD framework has been successfully applied to interpret galaxy clustering data from many galaxy surveys. For LAEs, the usual assumption in the HOD framework that galaxy properties are only a function of halo mass and are independent of large-scale environments breaks down, as a result of the selection caused by environment dependent Lyα RT. As shown in Section 4, the HOD of LAEs is strongly dependent on environments. Hamana et al. (2004) perform (environment-independent) HOD modeling of the angular 2PCF of $z = 4.86$ LAEs in one Subaru Deep Field and find that the observed strong clustering cannot be reproduced by the model. Given the large sample variance in the small field and crude error estimate of the clustering measurement, however, it is not clear whether the failure of the model in this case is caused by the neglecting of the Lyα selection effect. Our study shows that to correctly model LAE clustering within the HOD framework, one has to extend the framework to incorporate the strong environment dependence of Lyα selection.

As discussed in Paper I, the uncertainties in our current model lie in the intrinsic Lyα luminosity and spectra, which deserve detailed investigation. By "intrinsic", we mean the properties of Lyα photons after escaping the ISM. The intrinsic Lyα luminosity is related to the SFR and the initial mass function of stars. If the model (luminosity-threshold) LAEs are matched to the observed LAEs in terms of the number density, the uncertainty in the intrinsic Lyα luminosity is largely removed in studying LAE clustering. On the other hand, the intrinsic spectrum of Lyα emission, especially the intrinsic line width, is an important factor in determining the strength of the Lyα selection effect. A larger intrinsic line width would lead to a weaker dependence of Lyα RT on environments (Paper I), which in turn would make the effects of Lyα RT on LAE clustering weaker. For example, we would see a less elongated pattern in the 3D 2PCF of LAEs with a larger intrinsic line width. The intrinsic line shape may also be modified by galactic winds, which can also affects the Lyα RT (e.g., Kunth et al. 1998; Atek et al. 2008) and the effect on clustering. If isotropic galactic winds shift the initial Lyα line by a few hundred $\mathrm{km\,s^{-1}}$, the coupling of observed Lyα emission to the environment can be weakened. However, galactic winds usually display a collimated bipolar pattern, and photons escaping in directions other than the bipolar direction may not achieve a large shift. High-resolution simulation of individual galaxies with galactic wind included is useful for further studying the effect of wind on the observational properties of LAEs. See the tests and discussions in Appendix D. Consequently, if galactic wind can have a strong effect, the strength of Lyα-selection-induced clustering effects would allow us to potentially constrain the intrinsic Lyα line width and shape of LAEs, which would otherwise be difficult to discern. For low-mass halos ($\sim 10^{10} h^{-1} M_\odot$) in the simulation, the grid for hydrodynamic calculation marginally resolves the virial radius. The Lyα RT for sources in these halos may be limited by the resolution. However, the infall region (inside the turnaround radius), which is about 5.6 times larger and is important in shaping the Lyα RT, is well resolved. Therefore, the Lyα RT for sources in these low-mass halos is not expected to suffer the resolution effect significantly.

Lyα RT is a physical process that must exist around LAEs. The new effects on LAE clustering, including the enhancement in the projected 2PCFs, are strong, which means that they cannot be easily masked by other effects. If observation showed a null detection of the effects, e.g., finding no enhancement in the angular 2PCFs, it would have important implications in our study of LAEs. A substantial scatter in the intrinsic Lyα emission properties at fixed halo mass remains as a possibility to reduce or even mask the Lyα RT selection effect. In our model, the intrinsic Lyα emission properties, especially the Lyα luminosity, are tightly correlated with halo mass. The Lyα luminosity is based on the SFR averaged over 10Myr time scale and the star formation prescription does not lead to significant scatter in the SFR at fixed halo mass and redshift (Trac & Cen 2007). To have a large scatter in the instantaneous SFR, one needs to introduce a broad distribution of the star formation efficiency or make the star formation stochastic in halos of fixed mass. Dust in the ISM could further enlarge the scatter in the Lyα luminosity. If in the end the intrinsic Lyα luminosity distribution at fixed halo mass were much broader than that from Lyα RT effect (Paper I), the Lyα RT selection could be masked. In Appendix D, we present simple tests on the effect of the dispersion in the relation between intrinsic Lyα luminosity and halo mass. The dispersion can change the clustering amplitude of LAEs of fixed number density by including LAEs residing in lower mass halos. However, the anisotropic clustering pattern persists even if a large dispersion (1 dex in luminosity) is introduced. A broad or stochastic Lyα luminosity distribution would give rise to an effective duty cycle such that only a tiny fraction of galaxies are in the Lyα emitting phase at a given time, which means that at a given number density LAEs reside in halos of much lower mass, compared to the case of a narrow intrinsic Lyα luminosity distribution to start with. Nagamine et al. (2010) argue that a duty cycle scenario provides a reasonable explanation to existing LAE clustering measurements. To fully address the magnitude of the distribution and stochasticity of star formation efficiency, the relevant processes have to be incorporated in the reionization simulation, which is limited by our understanding of baryon physics. Potential consequences, when combined with Lyα RT selection, on LAE clustering deserves detail investigations. Strong tests to the model and constraints on different processes are expected to come from the Lyα LF, UV LF, and clustering of LAEs.

The completely new effects on LAE clustering due to Lyα RT add another layer of complexity in modeling their clustering. This means that the existence of Lyα selection effect would complicate the inference of cosmological parameters from LAE clustering in large LAE surveys. To map from galaxy clustering to dark matter clustering, which directly encodes the cosmological information, the effects that are commonly considered in current galaxy clustering analysis include the redshift-space distortion, the nonlinear evolution of structure, and the scale-dependent bias induced by halo biasing. For Lyα selected galaxies, the new effects that add to the above list are the anisotropic clustering (opposite to and stronger than the redshift-space distortion) and the scale-dependent bias induced by environment-dependent Lyα RT. For our model with $z = 5.7$ LAEs, the Lyα-selection-induced anisotropy is overwhelming.

At lower redshifts $z = 2 - 3$ we expect the Lyα RT induced selection effect to continue to operate in the regions surrounding galaxies, as at $z = 5.7$ shown here. However, at present, it is not clear what the strength of the Lyα selection effect will be and up to what scales the clustering of LAEs is affected at these redshifts. Several competing factors prevents us from having a simple guess. On one hand, lower matter density and higher UV background at $z = 2 - 3$ (hence lower neutral hydrogen fraction in the scattering regions), compared to $z = 5.7$, permit easier escape of Lyα photons through the circum-galactic and inter-galactic gas. On the other hand, a lower Hubble velocity may provide a countering factor. We reserve a more detailed investigation of clustering of LAEs at $z = 2 - 3$ for a future work.

The strong environmental dependence of the Lyα selection, on the other hand, provides a sensitive way to probe the late stage of cosmological reionization. With simple treatments of Lyα RT, it has been shown that Lyα emission from LAEs can be used to probe the mean hydrogen neutral fraction as a function of redshift (e.g., from the Lyα LF; Malhotra & Rhoads 2004; Haiman & Cen 2005). Both Furlanetto et al. (2006) and McQuinn et al. (2007) show that the clustering of LAEs is enhanced by the patchy reionization. Our current work is limited to $z = 5.7$, when the reionization is completed, and we plan to perform full RT modeling of LAEs at higher redshifts in a subsequent paper. Because of the fast evolution of neutral hydrogen density as reionization proceeds, we would see a rapid change in the distribution of the observed-to-intrinsic Lyα luminosity ratio, which would lead to a rapid change in the clustering amplitude of LAEs relative to the underlying population (Furlanetto et al. 2006). The isolated H II bubbles introduce a characteristic scale, which would result in a scale dependence in the bias factor (Furlanetto et al. 2006). We also expect that isolated H II bubbles and large-scale fluctuations of photoionization rate may introduce additional effects in the 3D anisotropic clustering of LAEs. As a whole, we expect that different features in the clustering of LAEs, if detected, would provide a wealth of information about reionization.

We are grateful to David Weinberg for useful discussions and comments and for suggesting the use of shuffled samples. We thank Mark Dijkstra, Matt McQuinn, and Masami Ouchi for helpful discussions and comments on an earlier draft. We thank the referee for constructive comments. Z.Z. thanks Aaron Bray for useful discussions. Z.Z. gratefully acknowledges support from Yale Center for Astronomy and Astrophysics through a YCAA fellowship. Z.Z. also thanks Aspen Center for Physics for a stimulating atmosphere and Stuart Wyithe, Andrei Mesinger, and Paul Shapiro for interesting discussions. This work is supported in part by NASA grant NNG06GI09G and NNX08AH31G. H.T. is supported by an Institute for Theory and Computation Fellowship. J.M. is supported by the International Reintegration Grant of the European Research Council 2006-046435 and Spanish grant AYA2009-09745. J.M. thanks the Institute for Advanced Study for their hospitality. Computing resources were in part provided by the NASA High-End Computing (HEC) Program through the NASA Advanced Supercomputing (NAS) Division at Ames Research Center. The Lyα RT computations were performed at the Princeton Institute for Computational Science and Engineering (PICSciE). Z.Z. thanks Daisuke Nagai for the use of the chimay computer for conducting some analyses presented in this paper.

APPENDIX

A. THE EXTENDED VERSION OF THE SIMPLE PHYSICAL MODEL

For LAEs, we have identified density, peculiar velocity, and their gradients as the main factors in transforming the intrinsic Lyα emission properties to the observed ones. The dependence of Lyα RT on these quantities imposes a selection function for the appearance of LAEs, which affects the clustering of LAEs. In the simple model of LAE clustering presented in Section 3.2, for simplicity we only include the density and line-of-sight velocity gradient to understand the main features in LAE clustering. For completeness, we add the other factors into the model here and follow Section 3.2 in presenting it.

We still consider the case that the selection function is a linear function of the environment variables. The real-space density of LAE galaxies is related to the matter density modified by the selection function,

$$\bar{n}_g(1+\delta_g) = q\bar{n}_0(1+b\delta_m) \times \left[1 + \tilde{\alpha}_1\delta_m + \tilde{\alpha}_2\frac{1}{Ha}\frac{\partial v_z}{\partial z} + \tilde{\alpha}_3\frac{1}{Ha}\left(\frac{\partial v_x}{\partial x} + \frac{\partial v_y}{\partial y}\right) + \tilde{\alpha}_4\frac{v_z}{Hr_H a} + \tilde{\alpha}_5 r_H\frac{\partial \delta_m}{\partial z}\right], \tag{A1}$$

where b is the bias factor for the underlying galaxy population (with mean number density $\bar{n}_0$) before the Lyα selection is imposed, $\bar{n}_g$ is the mean number density of galaxies that are selected as LAEs, and q is the overall fraction of galaxies that are selected as LAEs, $\tilde{\alpha}_i$ (i=1, 2, 3, 4, and 5) are coefficients (assumed to be constant) in the selection function, r_H is a length scale introduced to make the coefficients dimensionless and is chosen to be the Hubble radius c/H when the scale factor is a. Note that unlike the simple model presented in Section 3.2, here we explicitly include the term (with coefficient $\tilde{\alpha}_3$) dependent on the transverse velocity gradient as well as that on the density (with coefficient $\tilde{\alpha}_1$), since they represent different physical effects (Section 2). The untilded and tilded coefficients have a simple relation. Since density and the divergence of velocity are connected from the continuity equation $\dot{\delta} + \nabla \cdot \mathbf{v}/a = 0$, we have $\alpha_1 = \tilde{\alpha}_1 - \tilde{\alpha}_3 f$ and $\alpha_2 = \tilde{\alpha}_2 - \tilde{\alpha}_3$ (see below). In equation (A1), $\tilde{\alpha}_1$ represent the selection effect purely caused by density and we expect it has a negative sign. Since higher line-of-sight velocity gradient corresponds to higher apparent-to-intrinsic Lyα luminosity ratio, the coefficient $\tilde{\alpha}_2$ should be positive. For reasons discussed in Section 2, the coefficient $\tilde{\alpha}_3$ is expected to be negative. The $\tilde{\alpha}_4$ term is related to the line-of-sight velocity, which is not an accurate description. The selection may only depend on the motion of the galaxy relative to its surrounding medium that scatters the Lyα photons, and a smoothing scale needs to be introduced in a full description. Here we simply include a $\tilde{\alpha}_4$ term to gain a rough idea on the possible effect.

Keeping the first order terms in Equation (A1) and noticing that $\bar{n}_g = q\bar{n}_0$, we have

$$\delta_g = (b + \tilde{\alpha}_1)\delta_m + \tilde{\alpha}_2 \frac{1}{Ha}\frac{\partial v_z}{\partial z} + \tilde{\alpha}_3 \frac{1}{Ha}\left(\frac{\partial v_x}{\partial x} + \frac{\partial v_y}{\partial y}\right) + \tilde{\alpha}_4 \frac{v_z}{Hr_H a} + \tilde{\alpha}_5 r_H \frac{\partial \delta_m}{\partial z}. \tag{A2}$$

By using $\delta_m = \sum_{\mathbf{k}} \delta_{m,\mathbf{k}} \exp(i\mathbf{k}\cdot\mathbf{r})$, $\partial\delta_m/\partial z = \sum_{\mathbf{k}} ik_z \delta_{m,\mathbf{k}} \exp(i\mathbf{k}\cdot\mathbf{r})$, $v_z = \sum_{\mathbf{k}} ifHak_z/k^2 \delta_{m,\mathbf{k}} \exp(i\mathbf{k}\cdot\mathbf{r})$, and $\partial v_z/\partial z = -\sum_{\mathbf{k}} fHa(k_z^2/k^2)\delta_{m,\mathbf{k}} \exp(i\mathbf{k}\cdot\mathbf{r})$, we can express the above relation in Fourier space as

$$\delta_{g,\mathbf{k}} = \left[(b + \tilde{\alpha}_1) - \tilde{\alpha}_2 f\mu^2 - \tilde{\alpha}_3 f(1-\mu^2) + i\left(\tilde{\alpha}_4 \frac{f}{kr_H} + \tilde{\alpha}_5 k r_H\right)\mu\right]\delta_{m,\mathbf{k}}. \tag{A3}$$

Redshift-space distortion contributes to the μ^2 term, and in redshift space, it reads

$$\delta^s_{g,\mathbf{k}} = \left[(b + \tilde{\alpha}_1 - \tilde{\alpha}_3 f) + (1 - \tilde{\alpha}_2 + \tilde{\alpha}_3) f\mu^2 + i\left(\tilde{\alpha}_4 \frac{f}{kr_H} + \tilde{\alpha}_5 k r_H\right)\mu\right]\delta_{m,\mathbf{k}}. \tag{A4}$$

Although $\tilde{\alpha}_1$ is expected to be negative, the combination $(\tilde{\alpha}_1 - \tilde{\alpha}_3 f)$ should be positive, according to Figure 2. Since the overall clustering effect is opposite to the linear redshift-space distortion, we expect $(\tilde{\alpha}_2 - \tilde{\alpha}_3)$ to be positive. The dependence of the selection on line-of-sight velocity and line-of-sight density gradient leads to phase shifts in the fluctuation.

With Equation (A4), the power spectrum of LAEs in redshift space is then

$$P^s_g(\mathbf{k}) = \left\{\left[\left(1 + \frac{\tilde{\alpha}_1 - \tilde{\alpha}_3 f}{b}\right) + (1 - \tilde{\alpha}_2 + \tilde{\alpha}_3)\beta\mu^2\right]^2 + \left(\tilde{\alpha}_4 \beta \frac{1}{kr_H} + \frac{\tilde{\alpha}_5}{b} k r_H\right)^2 \mu^2\right\} b^2 P_m(\mathbf{k}). \tag{A5}$$

This full expression of power spectrum includes both redshift distortion and Lyα selection effects. Compared to Equation (9), it has more terms to represent different physical effects in the selection. Setting all the coefficients $\tilde{\alpha}_i$ to zero gives the usual redshift space linear power spectrum. The dependence of Lyα RT on the velocity gradient leads to the same form of angular dependence as the redshift distortion in the anisotropic power spectrum, but with an opposite sign. The dependences on line-of-sight velocity and line-of-sight gradient of density (the $\tilde{\alpha}_4$ and $\tilde{\alpha}_5$ terms in Equation (A5) also contribute to the anisotropy. Furthermore, these dependences lead to scale-dependent bias for the power spectrum, with the velocity and density gradient terms dominant on large and small scales, respectively.

The monopole, quadrupole, and hexadecapole moments of the power spectrum in Equation (A5) are

$$P_0(k) = \left[\left(1 + \frac{\tilde{\alpha}_1 - \tilde{\alpha}_3 f}{b}\right)^2 + \frac{2}{3}\left(1 + \frac{\tilde{\alpha}_1 - \tilde{\alpha}_3 f}{b}\right)(1 - \tilde{\alpha}_2 + \tilde{\alpha}_3)\beta + \frac{1}{5}(1 - \tilde{\alpha}_2 + \tilde{\alpha}_3)^2\beta^2 + \frac{1}{3}\left(\tilde{\alpha}_4 \beta \frac{1}{kr_H} + \frac{\tilde{\alpha}_5}{b} k r_H\right)^2\right] b^2 P_m(k), \tag{A6}$$

$$P_2(k) = \left[\frac{4}{3}\left(1 + \frac{\tilde{\alpha}_1 - \tilde{\alpha}_3 f}{b}\right)(1 - \tilde{\alpha}_2 + \tilde{\alpha}_3)\beta + \frac{4}{7}(1 - \tilde{\alpha}_2 + \tilde{\alpha}_3)^2\beta^2 + \frac{2}{3}\left(\tilde{\alpha}_4 \beta \frac{1}{kr_H} + \frac{\tilde{\alpha}_5}{b} k r_H\right)^2\right] b^2 P_m(k), \tag{A7}$$

and

$$P_4(k) = \frac{8}{35}(1 - \tilde{\alpha}_2 + \tilde{\alpha}_3)^2 \beta^2 b^2 P_m(k). \tag{A8}$$

The changes in these multipole moments with respect to the redshift-distortion-only case ($\tilde{\alpha}_i = 0$) can be clearly seen. The monopole and quadrupole are affected by all the Lyα selection factors, while the hexadecapole only has additional contributions from the dependence on velocity gradient.

B. POWER SPECTRUM OF LAEs

In Section 3, we present the LAE clustering results in the form of 2PCFs, which are commonly measured in LAE surveys. In the simple model we develop, however, the clustering is easily studied in terms of the power spectrum, the counterpart of the 2PCF in Fourier space. To be in parallel with the physical model and for a better comparison, we present the power spectrum of model LAEs measured for a couple of samples.

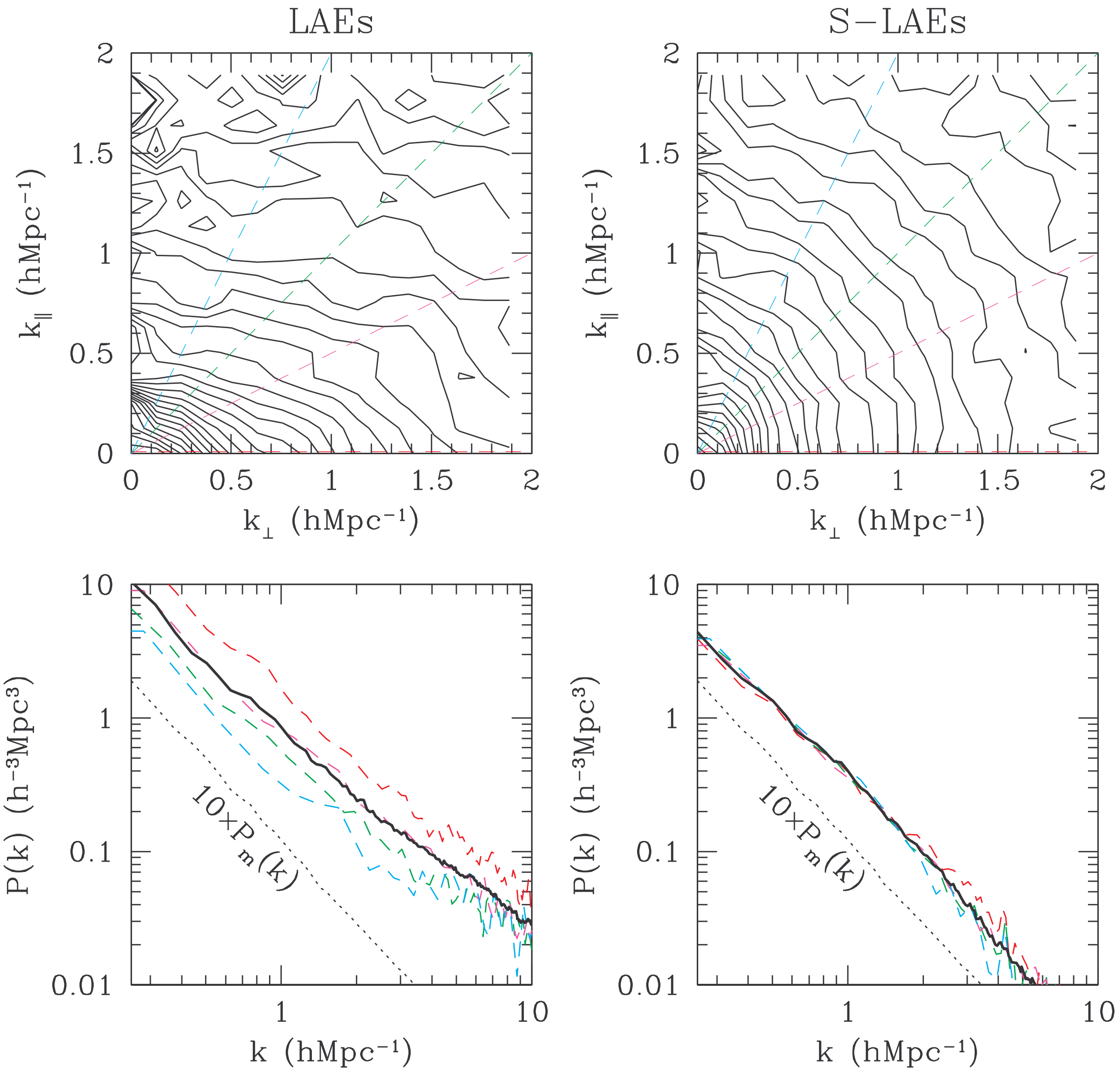

Fig. 19.— Redshift-space power spectra of LAEs (left) and S-LAEs (right). The LAE and S-LAE samples are Lyα luminosity-threshold samples of number density $10^{-2}h^3\mathrm{Mpc}^{-3}$. The S-LAE sample eliminates the environment effect of Lyα selection. For each column, the top panel shows the 3D redshift-space power spectra. Adjacent contours differ by 0.1dex in contour levels. The color coded dashed lines are four directions of wave vector. The power spectra along the four directions are compared in the bottom panel (dashed curves). The solid black curve in the bottom panel are the spherically averaged power spectrum and the dotted curve is the matter power spectrum.

For a given sample of LAEs, we derive a density field from the spatial distribution of LAEs using cloud in cell weighting. The density field in the simulation box ($100h^{-1}$Mpc on a side) is put into a 768^3 grid, the same size as the grid used in our RT calculation. We then perform fast Fourier transform (FFT) with the density grid to obtain the fluctuation power spectrum $P(\mathbf{k})$ of LAEs. To correct for the shot noise contribution to the power spectrum and the alias effect in the shot noise (Jing 2005), we generate 16 random catalogs in boxes of $100h^{-1}$Mpc on a side. The number of particles in each random catalog is the same as that of LAEs in consideration. The shot noise power spectrum of each random catalog is calculated from FFT. The average shot noise spectrum over the 16 realizations is subtracted from the above measured power spectrum of LAEs to obtain the final power spectrum. We also compute the power spectrum $P_m(k)$ of matter with FFT from the grid of matter density field.

The top-left panel of Figure 19 shows the (apparent) redshift-space 3D power spectrum $P(\mathbf{k})$ of the luminosity-threshold sample of LAEs with number density $10^{-2}h^3\mathrm{Mpc}^{-3}$. The line-of-sight elongation pattern seen in the 2PCF now corresponds to the squashed contours in the power spectrum plot. For comparison, the S-LAE sample of the same number density only shows a weak redshift-space distortion pattern (top-right panel of Figure 19), with contours slightly elongated along the line of sight. For a better comparison and to see the shape of $P(\mathbf{k})$ more clearly, we plot the power spectra at different angles with respect to the line of sight in the bottom panels of Figure 19 for the LAE and S-LAE samples, respectively. The curves are color coded in the same way as the directions of wave vectors shown in the top panels. The solid black curve in each of the bottom panels is the spherically averaged power spectrum.

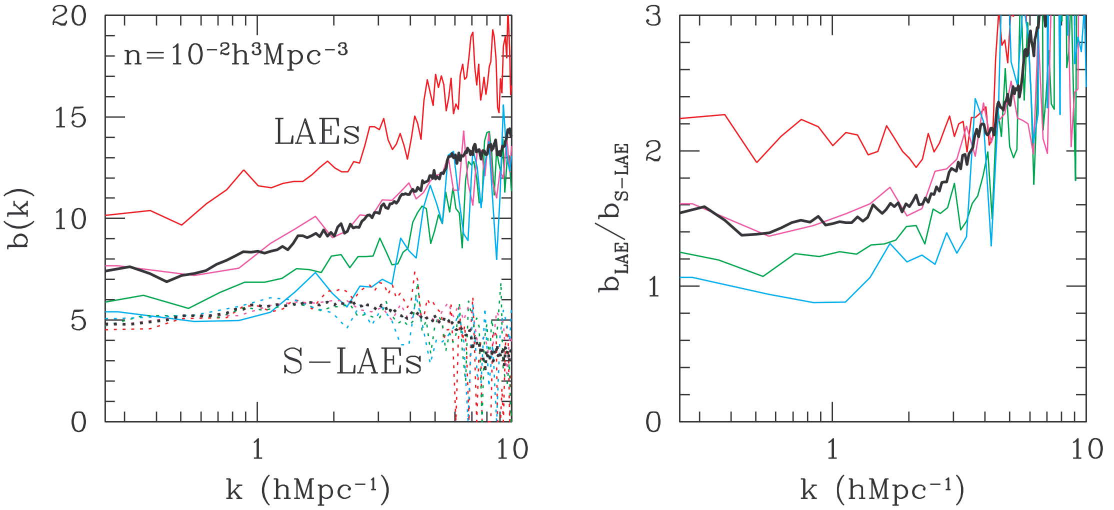

FIG. 20.— Scale dependence of the LAE bias factor. In the left panel, the solid (dotted) curves are the galaxy bias factors of LAEs (S-LAEs) at different directions, color coded in the same fashion as in Figure 19. The scale dependence seen in the S-LAE bias is caused by nonlinear structure growth, while that in the LAE bias is a combination effect of nonlinear growth and Lyα selection. In the right panel, the relative bias factors of LAEs and S-LAEs are plotted and the scale dependence seen here is supposed to be induced only by the Lyα selection effect. The number density of the luminosity-threshold LAE or S-LAE sample is $10^{-2}h^3\mathrm{Mpc}^{-3}$.

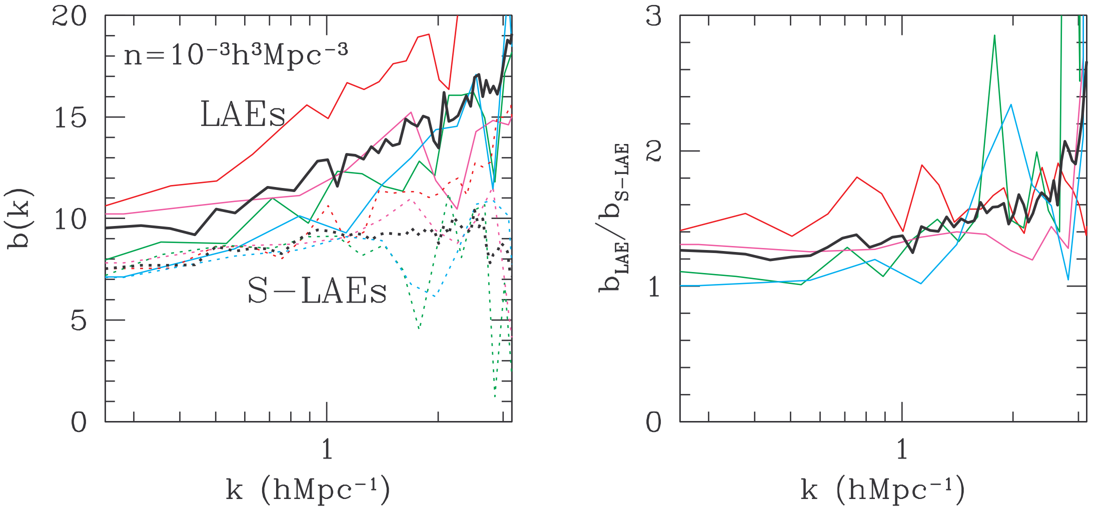

FIG. 21.— Same as Figure 20, but for samples of number density $10^{-3}h^3\mathrm{Mpc}^{-3}$. Note that the upper limits in k differ from those in Figure 20 to avoid plotting noisy data.

For S-LAEs, the Lyα selection effect is eliminated and only redshift-space distortion effect is left. Since the sample is highly biased, the redshift-space distortion parameter $\beta = \Omega^{0.6}/b$ is small and the redshift-space distortion effect is weak. In the bottom-right panel, we only see small differences in the $P(\mathbf{k})$ at different angles, or at different values of μ (the cosine of the angle between the line of sight and the wave vector). The shape of $P(\mathbf{k})$ reflects that of halos. It shows slight difference from the matter power spectrum $P_m(k)$, which results from nonlinear structure growth and halo biasing.

For LAEs, the anisotropy caused by Lyα selection is very strong (dashed curves in the bottom-left panel). The amplitude of $P(\mathbf{k})$ continuously increases as the direction of the wave vector gets closer to the line of sight, i.e., as the value of μ becomes larger. This is in line with the trend from the physical model (Equation (A5)). The shape of $P(\mathbf{k})$ shows a clear departure from that of $P_m(k)$, which is predicted by the physical model as the results of the dependence of Lyα selection on the line-of-sight velocity and line-of-sight density gradient. The departure is larger at smaller scales (larger k), which implies that the effect of line-of-sight density gradient (the $\tilde{\alpha}_5$ term Equation (A5)) likely dominates the scale dependence.

To clearly see the scale dependence, we plot the galaxy bias factor at different values of μ as a function of scale in the left panel of Figure 20. We compute the galaxy bias factor as the square root of $P(\mathbf{k})/P_m(k)$. For S-LAEs (dotted curves), the deviation from a constant bias factor is a result of nonlinear structure growth and halo biasing. For LAEs (solid curves), the deviation is a combination of the above effects and the Lyα selection effect. If we take the ratio of the bias factors of LAEs and S-LAEs at different values of μ, we can remove the effect only caused by nonlinear structure growth and halo biasing. The right panel of Figure 20 shows such relative bias factors of LAEs and S-LAEs. The scale dependence in this panel is introduced by the selection effect from environment-dependent Lyα RT. We can see the trend that the scale dependence is stronger at higher values of μ, in a qualitative agreement with the simple model (Equation (A5)).

Figure 21 shows the scale dependence of the bias factors of LAE and S-LAE samples with a lower number density ($10^{-3}h^3\mathrm{Mpc}^{-3}$). Since the samples correspond to more massive halos, it is not surprising that the scale dependence caused by nonlinear structure growth and halo biasing becomes stronger, as seen in the bias factors of S-LAEs (dotted curves in the left panel). The Lyα-selection-induced scale dependence and the trend with μ can still be clearly seen (right panel). Compared with the $10^{-2}h^3\mathrm{Mpc}^{-3}$ case, the bias factor of LAEs with the lower number density shows a weaker dependence on μ. In the simple model, this can be largely explained by the larger value of b in Equation (A5).

The overall trends seen in the power spectrum of LAEs seem to be captured by the extended simple model. Therefore, the simple model can be used for qualitative understanding of LAE clustering.

C. CLUSTERING OF LAEs IN THE $\exp(-\tau_\nu)$ MODEL

In this Appendix, we compare the predictions of clustering of LAEs in the full Lyα RT model and the $\exp(-\tau_\nu)$ model.

The $\exp(-\tau_\nu)$ model is adopted in previous work for the Lyα RT calculation, which computes the line-of-sight optical depth τ_ν to a source and modifies the intrinsic Lyα emission by the $\exp(-\tau_\nu)$ factor. The $\exp(-\tau_\nu)$ model is reasonably accurate in describing Lyα absorption feature for Lyα photons passing through neutral clouds/islands, especially for absorption caused by the damping wing or small optical depth. In the case of studying the observed Lyα emission, as shown in Paper I, the $\exp(-\tau_\nu)$ model can qualitatively explain some trends in the Lyα flux suppression, but it cannot provide quantitative results because of the lack of frequency diffusion and spatial diffusion in the model. Previous work intends to limit the $\exp(-\tau_\nu)$ model to study the transfer outside of a radius much larger than halo size by assuming a Lyα line profile at that radius. Even if this is the case, it is not clear what radius to use, what line profile to assume, and what angular distribution of Lyα emission at that radius to adopt, which all rely on the Lyα RT inside that radius. Here we take the original meaning of the $\exp(-\tau_\nu)$ model and compute the line-of-sight optical depth τ_ν all the way to the source.

As discussed in Section 2, the line-of-sight optical depth is not the single factor in determining the Lyα RT, since scatterings of Lyα photons enable them to probe the optical depth in all directions. The $\exp(-\tau_\nu)$ model does not fully take into account the environment around the source. It fails to even qualitatively reproduce the trend of the Lyα flux suppression with density at fixed line-of-sight gradient, as seen in Figure 2.

Since $\exp(-\tau_\nu)$ model still partially captures the environment effect on Lyα RT, the new effects in LAE clustering predicted by our full Lyα RT model are expected to be more or less seen in this model. Here, we compare the clustering properties of LAEs in the full RT and $\exp(-\tau_\nu)$ models for samples defined by thresholds in observed Lyα luminosity. With the same initial setups (i.e., intrinsic Lyα luminosity and line profile) as in our full RT calculation, the $\exp(-\tau_\nu)$ model underpredicts the observed Lyα luminosity (Paper I). We also include a case of $\exp(-\tau_\nu)$ model with higher intrinsic Lyα line width σ_{init}, corresponding to the circular velocity at halo virial radius. The apparent Lyα LF from this $\exp(-\tau_\nu)$ model roughly match what we obtain from the above full RT model. We construct luminosity threshold LAE samples from the three models to have the same number density.

Figure 22 compares the spatial distributions and the 3D 2PCFs for LAEs of number density $5\times10^{-3}h^3\mathrm{Mpc}^{-3}$ in the three models. The line-of-sight elongation pattern is also seen in the $\exp(-\tau_\nu)$ models (middle-left and bottom-left panels). However, it is not as prominent as in the full RT model and it is weak in the high-σ_{init} model (bottom-left panel). Compared to shuffled samples (not shown here), LAEs in the $\exp(-\tau_\nu)$ models also show enhanced clustering in the transverse plane. However, the clustering is not as strong as in the full RT model (see panels in the middle row). In terms of the reals-pace 3D 2PCFs, LAEs show a stronger clustering and a more prominent line-of-sight elongation feature in the full RT model than in the $\exp(-\tau_\nu)$ models.

Figure 23 compares the projected 2PCFs in the three models for three LAE samples with different number densities. The projected 2PCF appears to be flatter in the $\exp(-\tau_\nu)$ models than in the full RT model. The shape is more parallel to the matter 2PCF, which suggests a weaker scale dependence in the bias factor. LAEs from the high-σ_{init} $\exp(-\tau_\nu)$ model shows a much weaker clustering than those from the full RT model. The large scale bias factor of LAEs in the $\exp(-\tau_\nu)$ models relative to halos has a similar trend as seen in Figure 15.

Our comparison shows that it may be possible to adjust the intrinsic Lyα line width in the $\exp(-\tau_\nu)$ model to approximately match the apparent Lyα LF, but the clustering of LAEs would be far off. Alternatively, the intrinsic Lyα line width could be adjusted to roughly match the clustering, but the apparent Lyα LF would be far off. The $\exp(-\tau_\nu)$ model cannot fit both the apparent Lyα LF and the clustering of LAE.

As a whole, the Lyα selection effects on clustering are preserved to some extent in the $\exp(-\tau_\nu)$ model. The reason may lie in that the Lyα optical depth is strongly dependent on the velocity gradient, which plays a major role in determining the anisotropic distribution of Lyα emission of a LAE source (see the illustration in Figure 9) and in driving the anisotropic clustering of LAEs (Section 3.2). The line-of-sight optical depth computed in the $\exp(-\tau_\nu)$ model encodes the information of the line-of-sight velocity gradient, so it is not surprising that the model is able to qualitatively captures the main effects of Lyα selection in LAE clustering.

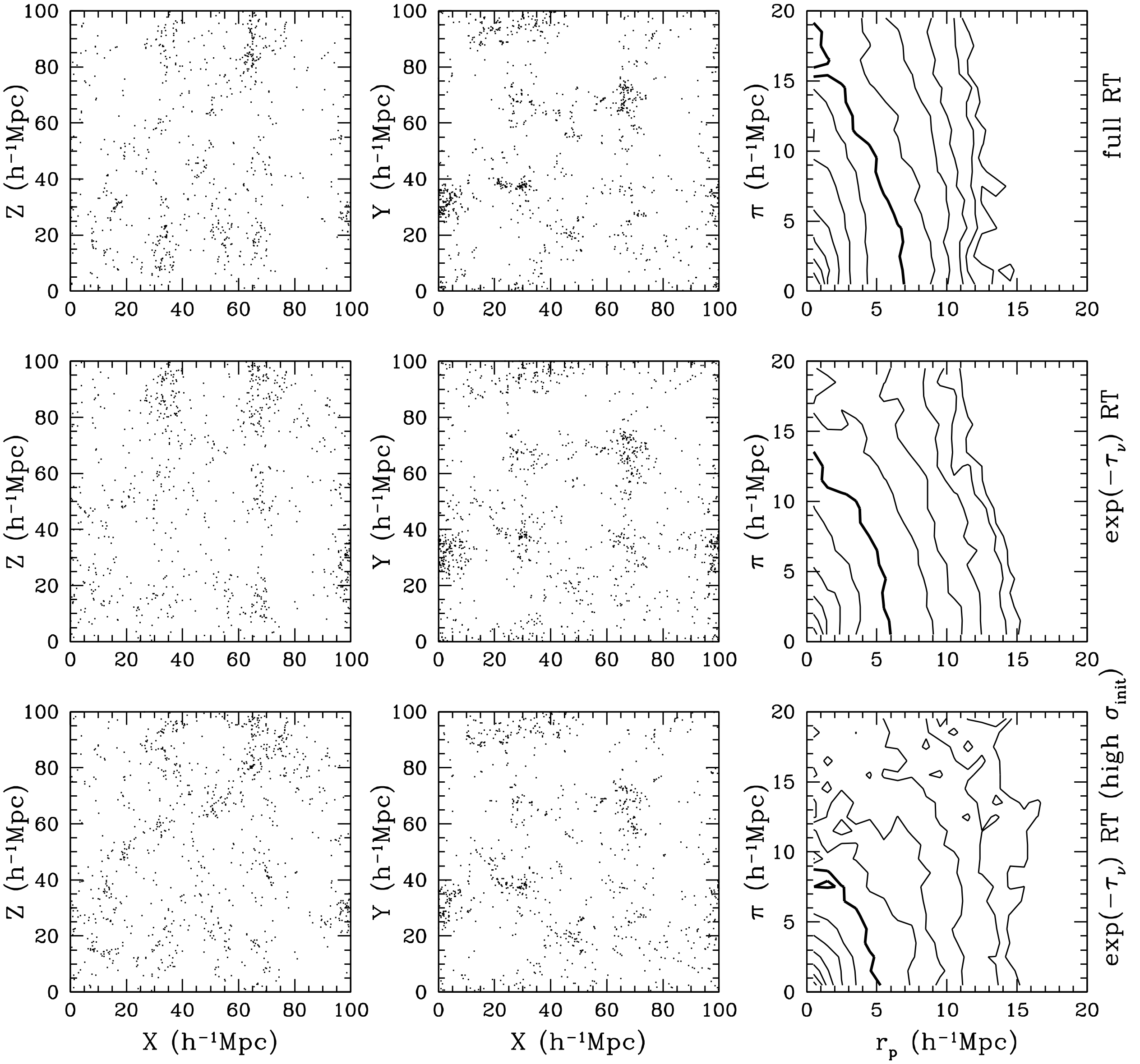

FIG. 22.— Spatial distributions of LAEs and 3D 2PCFs in real space in the full Lyα RT model (top row) and two $\exp(-\tau_\nu)$ RT models (middle and bottom rows). The LAE samples from the three models are defined by thresholds in observed Lyα luminosity so that they have the same number density, $5\times10^{-3}h^3\mathrm{Mpc}^{-3}$. The $\exp(-\tau_\nu)$ RT model in the middle row adopts the same intrinsic Lyα line width as the full RT model, which cannot produce an apparent Lyα LF that matches that from the full RT model. The $\exp(-\tau_\nu)$ RT model in the bottom row adopts a larger intrinsic Lyα line width so that it roughly produces an apparent Lyα LF matching that from the full RT model. Left panels compare the distributions with one spatial direction along the line of sight. The observer is supposed to be on the top of the panels. Middle panels compare the distributions in the transverse plane perpendicular to the line of sight. The corresponding slices from the three models are from the same part of the box, with a thickness of $20h^{-1}$Mpc. Right panels compare the real-space 3D 2PCFs of LAEs from the three models. The solid contour in each panel denotes a contour level of unity, and the adjacent contours differ by 0.2dex in contour levels.

However, the $\exp(-\tau_\nu)$ model excludes the environment information in directions other than the line of sight. Furthermore, the effect of velocity gradient in this model is computed with the initial line profile, despite that the line profile changes because of frequency diffusion caused by scatterings around the source. The model therefore cannot give a full description of Lyα selection effect on environment and cannot explain the observed LAE properties (e.g., Lyα LF and clustering) quantitatively and self-consistently.

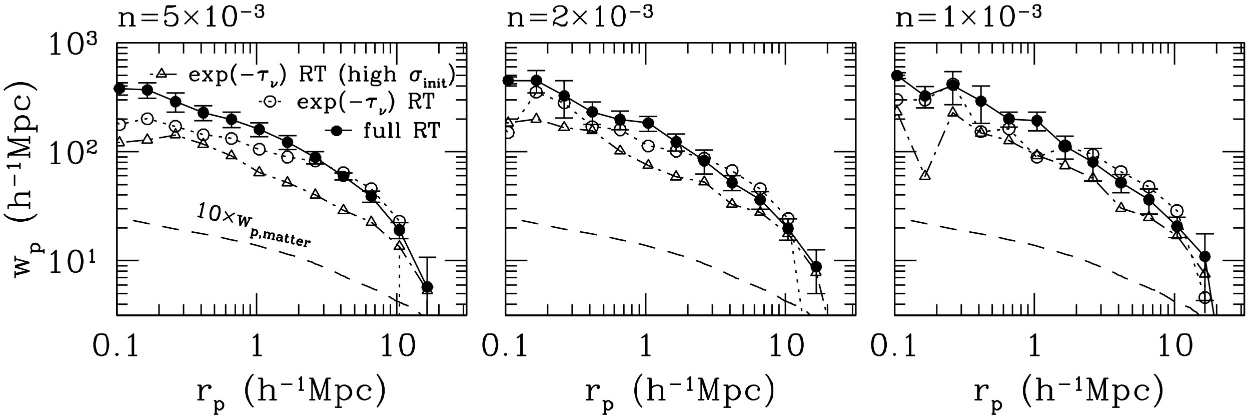

FIG. 23.— Projected 2PCFs of LAEs in the full Lyα RT model and two $\exp(-\tau_\nu)$ RT models. In each panel, the LAE samples from the three models are defined by thresholds in observed Lyα luminosity so that they have the same number density (marked on top of the panel in units of $h^3\mathrm{Mpc}^{-3}$). The dashed curve is the projected 2PCF of matter, scaled by a factor of 10. The $\exp(-\tau_\nu)$ RT model with open circles adopts the same intrinsic Lyα line width as the full RT model, which cannot produce an apparent Lyα LF that matches that from the full RT model. The $\exp(-\tau_\nu)$ RT model with open triangles adopts a larger intrinsic Lyα line width so that it roughly produces an apparent Lyα LF matching that from the full RT model.

D. EFFECTS OF THE INTRINSIC Lyα LINE PROFILE AND THE DISPERSION BETWEEN INTRINSIC LUMINOSITY AND HALO MASS

In this appendix, we first show the effect of the intrinsic Lyα line profile on the scattered Lyα emission and discuss how it may affect the clustering of LAEs. We then investigate how a scatter in the intrinsic Lyα (or UV) luminosity and halo mass relation may change the clustering effects caused by the Lyα RT.

As mentioned in Paper I, one main uncertainty in the the RT model of LAEs is the initial or intrinsic Lyα line profile (after Lyα photons escape the ISM). In our current setup, the profile is assumed to be Gaussian with the width determined by the thermal temperature of the host halo. In reality, the shape and width of the intrinsic Lyα line are determined by gas dynamics in galaxies and affected by galaxy disk rotation, galaxy merging, and galactic wind. As a result, the Lyα line can be broadened, become asymmetric, and/or have a shift in wavelength. All of these effects may change the strength of the coupling between observed Lyα properties and circum-galactic and inter-galactic environments, and therefore have an impact on the clustering effects discussed in this paper.

A thorough investigation on the effect of the intrinsic line profile is out of the scope of this paper. Here we present a test to show how sensitive the observed Lyα emission is to the change in the initial Lyα line wavelength. We perform RT calculations for an individual source in a halo of $10^{11}h^{-1}M_\odot$ and consider cases with different initial values of Lyα wavelength. For each case, the initial Lyα photons all have a single wavelength with the luminosity normalized to be the intrinsic Lyα luminosity of the source. That is, the line follows the Dirac δ function.

In the left panel of Figure 24, the Lyα surface brightness profile of the source is shown for a few cases. The initial Lyα line wavelength is denoted by the wavelength shift relative to the rest-frame Lyα line center, in units of the halo thermal velocity dispersion $\sigma \simeq 70\mathrm{km\,s^{-1}}$.

On average, bluer initial Lyα photons lead to less concentrated surface brightness profile, since these photons need to travel farther in the IGM before they redshift into the line center to encounter significant scatterings. Redder initial photons make the profile more concentrated and more point-like, A small fraction of the initial red photons can blueshift to the line center by encountering scatterings in the infall region around the halos, which makes the profile still appear to be extended on large scales. The solid curves in the left panel of Figure 24 show that the profile is insensitive to the initial Lyα wavelength if the initial shifts of photons are within the $\pm 3\sigma$ range. These photons encounter a lot of core scatterings and redistribute their wavelength in the $\pm 3\sigma$ range, and therefore they lost their memory of the initial states.

In the right panel, we show the Lyα flux in a central $3''.5$ diameter aperture for different choice of the initial Lyα wavelength. The two curves in the upper panel are fluxes observed in opposite directions. The difference in the two curve tells us how anisotropic the scattered Lyα emission is and provides an estimate of the strength of the coupling between environments and scattered Lyα emission through RT. If the initial shift of photons is smaller than $\sim 3.5\sigma$, the flux from the central aperture is strongly suppressed. Meanwhile, there is a large difference in the fluxes observed from the two opposite directions. Both indicate the strong coupling between the observed Lyα emission and circum-galactic and inter-galactic environments. For photons with initial shift larger than $\sim 3.5\sigma$, a fraction of photons can be out of resonance in the circum-galactic and inter-galactic media, weakening the coupling. However, the fluxes in opposite directions still show $\sim$20% difference.

The above test seems to suggest that the environment-dependent RT effect becomes weak if the initial line shifts is larger than $\sim 3.5\sigma$ ($\sim 250\mathrm{km\,s^{-1}}$) for halos of $10^{11}h^{-1}M_\odot$. Galactic winds can have the effect of shifting Lyα emission toward red (e.g., Verhamme et al. 2006; Dijkstra & Wyithe 2010). Observationally, galactic winds are ubiquitous in star-forming galaxies. Steidel et al. (2010) find that the interstellar absorption lines and the Hα line have a mean shift

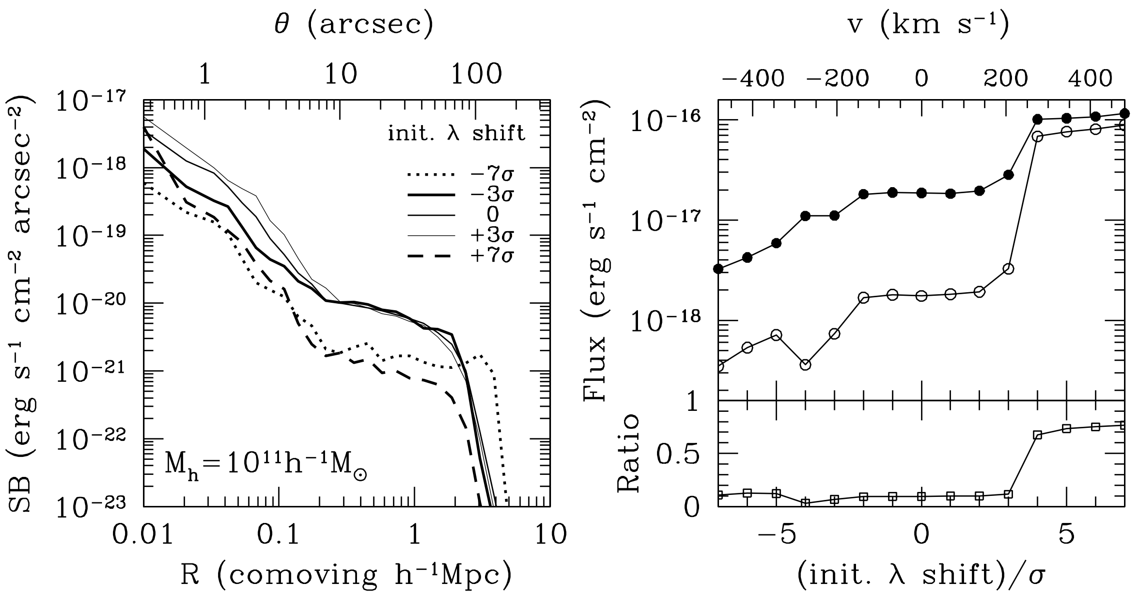

FIG. 24.— Effect of initial Lyα line wavelength shift on the Lyα flux distribution. The left panel shows the surface brightness profiles of the scattered Lyα emission for a source residing in a $10^{11}h^{-1}M_{\odot}$ halo, chosen from the simulation box. For each profile, the initial Lyα line from the central source has a single wavelength, denoted by the wavelength shift with respect to the rest-frame line center in units of the halo thermal velocity dispersion $\sigma \simeq 70\mathrm{km\,s}^{-1}$. The right panel shows the Lyα flux in a central $3''.5$ diameter aperture as a function of the initial Lyα wavelength shift. The two curves in the upper panel are for fluxes observed in opposite directions, and the curve in the lower panel shows their ratio.

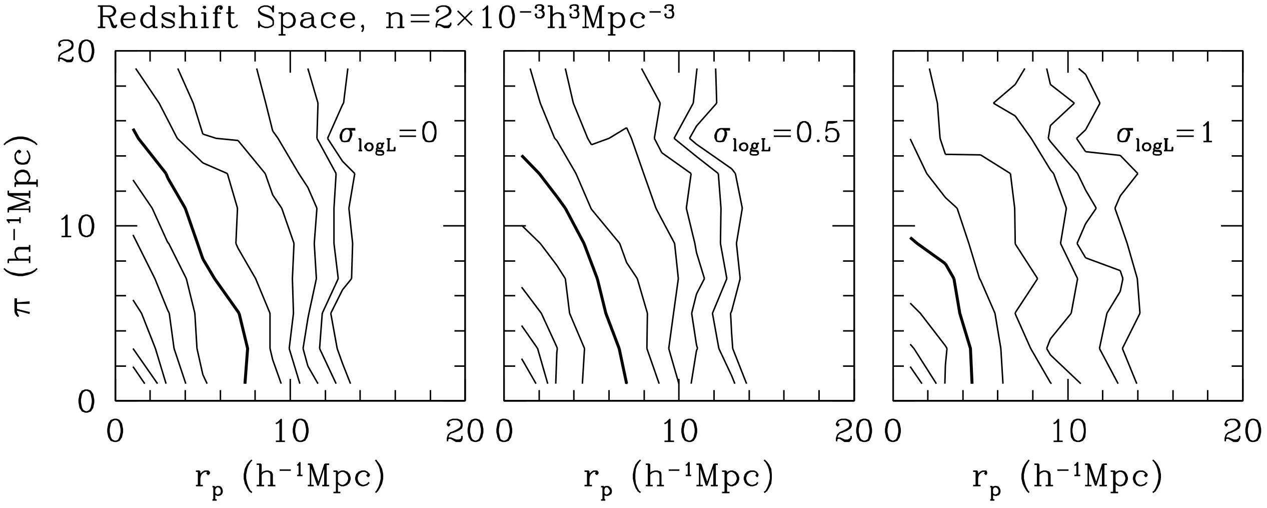

FIG. 25.— Effect of scatter between intrinsic Lyα luminosity $L_{\mathrm{intrinsic}}$ and halo mass on the 3D redshift-space 2PCFs of LAEs. A Gaussian distribution is introduced for $\log L_{\mathrm{intrinsic}}$ with standard deviation $\sigma_{\log L}$ and fixed mean. The LAE sample is constructed by selecting LAEs above a threshold in *observed* Lyα luminosity so that the number density is $2\times10^{-3}h^3\mathrm{Mpc}^{-3}$. From left to right, the cases for $\sigma_{\log L}$=0, 0.5, and 1 are shown, respectively. See the text for details.

of $\sim 160\mathrm{km\,s}^{-1}$ with a large scatter for $z \sim$ 2–3 Lyman break galaxies with *baryon* mass of $10^{10}-10^{11}M_{\odot}$. Such a wind velocity may be able to shift the Lyα line by a few hundred $\mathrm{km\,s}^{-1}$. However, the outflowing neutral gas of the wind is observed to be usually collimated in a bipolar fashion (e.g., Bland & Tully 1988; Shopbell & Bland-Hawthorn 1998; Veilleux & Rupke 2002). Lyα emission escaping in directions other than the wind is expected to have smaller redward shift, which can still probe the circum-galactic and inter-galactic environments through scatterings. Therefore, it is likely that the clustering features we study in this paper persist in the presence of galactic wind. Radiative transfer modeling of individual galaxies in high resolution simulations with galactic wind prescription will help to further shed light on this issue.

We now turn to discuss whether a dispersion in the intrinsic Lyα (UV) luminosity and halo mass can substantially weaken the RT caused clustering effects. With the star formation recipe in the cosmological reionization simulation, whose output we use for the RT calculation, the SFR and halo mass appear to be tightly correlated. In reality, star formation may be more stochastic as a result of feedback, merging, gas accretion, and so on, and the SFR (or intrinsic

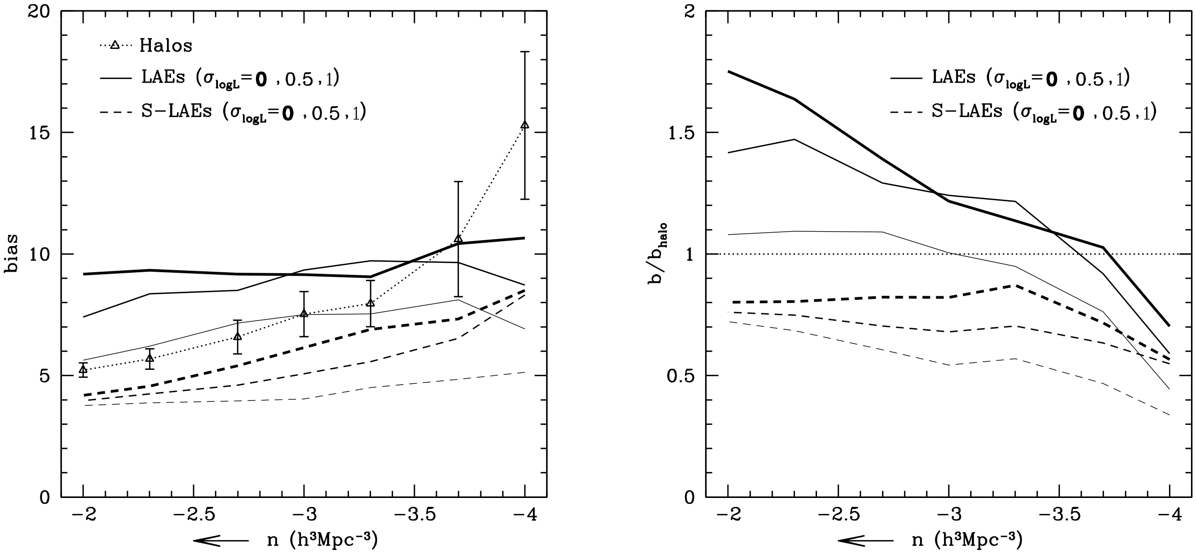

FIG. 26.— Effect of scatter between intrinsic Lyα luminosity $L_{\rm intrinsic}$ and halo mass on the bias factors of LAEs. A Gaussian distribution is introduced for $\log L_{\rm intrinsic}$ with standard deviation $\sigma_{\log L}$ and fixed mean. The left and right panels are for absolute bias factor and that relative to halos, similar to Figure 15. The bias curves are shown for both LAE and S-LAE samples, with $\sigma_{\log L}$=0, 0.5, and 1 (from thick to thin curves), respectively.

Lyα luminosity) at fixed halo mass may vary a lot from halo to halo. At a fixed observed Lyα luminosity, in addition to the RT caused mixing of host halo masses, we would have further mixing from the variation in the SFR. To see whether the stochastic star formation can wash out the clustering effects, we perform a simple test.

We introduce a log-normal dispersion in the intrinsic Lyα luminosity $L_{\rm intrinsic}$ and halo mass relation, characterized by the standard deviation $\sigma_{\log L}$ of $\log L_{\rm intrinsic}$. To obtain the observed Lyα luminosity, we assume that the observed-to-intrinsic Lyα luminosity ratio does not change for each individual halo. Strictly speaking, this assumption is not accurate, since the radius of the contour of the detection threshold surface brightness (see Paper I) changes as one varies the intrinsic luminosity of a source. To be accurate, one needs to redo the expensive RT calculation. However, the assumption suffices for our purpose to investigate the effect of the scatter. We construct LAE and S-LAE samples with different thresholds in the observed Lyα luminosity.

Figure 25 shows the 3D redshift-space 2PCFs for $n = 2 \times 10^{-3} h^3{\rm Mpc}^{-3}$ LAE samples, with $\sigma_{\log L}$=0 (no scatter, the default case in this paper), 0.5, and 1. At a fixed number density, a larger scatter brings a larger fraction of sources in low-mass halos into the sample, so the sample of LAEs would on average have a lower bias factor. We see that the clustering amplitude, indicated by the position of the thick solid curve, decreases as $\sigma_{\log L}$ increases. However, the elongation pattern along the line of sight, which is an indication of the environment dependent RT effect, remains clearly visible even for the case of $\sigma_{\log L} = 1$ (i.e., one order of magnitude variation in $L_{\rm intrinsic}$).

In Figure 26, we show the bias factor of LAEs and S-LAEs as a function of sample number density. From the left panel, the range of weak dependence of LAE clustering on sample number density tends to shift to lower number density for larger scatter $\sigma_{\log L}$. At higher number density, the weak dependence breaks down, and the bias factor shows a similar slope as the halo samples. The right panel displays the bias factor relative to the halo sample. It turns out to be always true that LAEs are more strongly clustered than the corresponding S-LAEs, which means that the RT caused selection effect remains strong even for the case of large scatter.

Our tests demonstrate that a large dispersion (up to $\sigma_{\log L} = 1$) in the intrinsic Lyα luminosity and halo mass relation cannot completely wash out the RT caused clustering effects studied in this paper.

REFERENCES

Atek, H., Kunth, D., Hayes, M., Östlin, G., & Mas-Hesse, J. M. 2008, A&A, 488, 491
Berlind, A. A. & Weinberg, D. H. 2002, ApJ, 575, 587
Bland, J., & Tully, B. 1988, Nature, 334, 43
Blanton, M. R., Eisenstein, D. J., Hogg, D. W., & Zehavi, I. 2006, ApJ, 645, 977
Croton, D. J., Gao, L., & White, S. D. M. 2007, MNRAS, 374, 1303
Dayal, P., Ferrara, A., & Gallerani, S. 2008, MNRAS, 389, 1683
Dayal, P., Ferrara, A., Saro, A., Salvaterra, R., Borgani, S., & Tornatore, L. 2009, MNRAS, 400, 2000
Dayal, P., Maselli, A., & Ferrara, A. 2010, MNRAS, in press (arXiv:1002.0839)
Dijkstra, M., Lidz, A., & Wyithe, J. S. B. 2007, MNRAS, 377, 1175
Dijkstra, M., Wyithe, J. S. B., & Haiman, Z. 2007, MNRAS, 379, 253
Dijkstra, M., & Wyithe, J. S. B. 2010, MNRAS, 408, 352
Dunkley, J., et al. 2009, ApJS, 180, 306
Eisenstein, D. J., et al. 2005, ApJ, 633, 560
Furlanetto, S.R., Zaldarriaga, M., & Hernquist, L. 2006, MNRAS, 365, 1012
Gao, L., & White, S. D. M. 2007, MNRAS, 377, L5
Gawiser, E., et al. 2007, ApJ, 671, 278
Guaita, L., et al. 2010, ApJ, 714, 255
Haiman, Z., & Cen, R. 2005, ApJ, 623, 627
Haiman, Z., & Spaans, M. 1999, ApJ, 518, 138

Hamana, T., Ouchi, M., Shimasaku, K., Kayo, I., & Suto, Y. 2004, MNRAS, 347, 813

Hamilton, A. J. S. 1998, The Evolving Universe, 231 (Dordrecht: Kluwer), 185

Hill, G. J., et al. 2008, in ASP Conf. Ser., 399 (San Francisco, CA: ASP), 115

Hirata, C. M. 2009, MNRAS, 399, 1074

Iliev, I. T., Shapiro, P. R., McDonald, P., Mellema, G., & Pen, U.-L. 2008, MNRAS, 391, 63

Jing, Y. P. 2005, ApJ, 620, 559

Kaiser, N. 1987, MNRAS, 227, 1

Kashikawa, N., et al. 2006, ApJ, 648, 7

Kunth, D., Mas-Hesse, J. M., Terlevich, E., Terlevich, R., Lequeux, J., & Fall, S. M. 1998, A&A, 334, 11

Kovač, K., Somerville, R. S., Rhoads, J. E., Malhotra, S., & Wang, J. 2007, ApJ, 668, 15

Landy, S. D., & Szalay, A. S. 1993, ApJ, 412, 64

Malhotra, S., & Rhoads, J. 2004, ApJ, 617, L5

McDonald, P. 2003, ApJ, 585, 34

McDonald, P., Miralda-Escudé, J., Rauch, M., Sargent, W. L. W., Barlow, T. A., Cen, R., & Ostriker, J. P. 2000, ApJ, 543, 1

McQuinn, M., Hernquist, L., Zaldarriaga, M., & Dutta, S. 2007, MNRAS, 381, 75

Mesinger, A., & Furlanetto, S.R. 2008, MNRAS, 386, 1990

Miralda-Escudé, J. 1998, ApJ, 501, 15

Miralda-Escudé, J., & Rees, M.J. 1998, ApJ, 497, 21

Murayama, T., et al. 2007, ApJS, 172, 523

Nagamine, K., Ouchi, M., Springel, V., & Hernquist, L. 2010, PASJ, in press (arXiv:0802.0228)

Orsi, A., Lacey, C. G., Baugh, C. M., & Infante, L. 2008, MNRAS, 391, 1589

Osterbrock, D. E. 1989, Astrophysics of Gaseous Nebulae and Active Galactic Nuclei (Mill Valley, CA: Univ. Sci. Books)

Ouchi, M., et al. 2003, ApJ, 582, 60

Ouchi, M., et al. 2008, ApJS, 176, 301

Ouchi, M., et al. 2010, ApJ, 723, 869

Padilla, N. D., Ceccarelli, L., & Lambas, D. G. 2005, MNRAS, 363, 977

Santos, M. R. 2004, MNRAS, 349, 1137

Shimasaku, K., et al. 2004, ApJ, 605, L93

Shopbell, P. L., & Bland-Hawthorn, J. 1998, ApJ, 493, 129

Steidel, C. C., Erb, D. K., Shapley, A. E., Pettini, M., Reddy, N., Bogosavljević, M., Rudie, G. C., & Rakic, O. 2010, ApJ, 717, 289

Takada, M., Komatsu, E., & Futamase, T. 2006, Phys. Rev. D, 73, 083520

Tilvi, V., Malhotra, S., Rhoads, J. E., Scannapieco, E., Thacker, R. J., Iliev, I. T., & Mellema, G. 2009, ApJ, 704, 724

Tinker, J. L., Conroy, C., Norberg, P., Patiri, S. G., Weinberg, D. H., & Warren, M. S. 2008, ApJ, 686, 53

Trac, H., & Cen, R. 2007, ApJ, 671, 1

Trac, H., Cen, R., & Loeb, A. 2008, ApJ, 689, L81

Veilleux, S., & Rupke, D. S. 2002, ApJ, 565, L63

Verhamme, A., Schaerer, D., & Maselli, A. 2006, A&A, 460, 397

Wang, J.-X., Malhotra, S., Rhoads, J. E., Zhang, H.-T., & Finkelstein, S. L. 2009, ApJ, 706, 762

Wechsler, R. H., Zentner, A. R., Bullock, J. S., Kravtsov, A. V., & Allgood, B. 2006, ApJ, 652, 71

Wyithe, J. S. B., & Cen, R. 2007, ApJ, 659, 890

Yoo, J., Tinker, J. L., Weinberg, D. H., Zheng, Z., Katz, N., & Davé, R. 2006, ApJ, 652, 26

Zheng, Z. 2004, ApJ, 614, 527

Zheng, Z., & Miralda-Escudé, J. 2002, ApJ, 578, 33

Zheng, Z., et al. 2005, ApJ, 633, 791

Zheng, Z., Cen, R., Trac, H., & Miralda-Escudé, J. 2010, ApJ, 716, 574

Zheng, Z., Coil, A. L., & Zehavi, I. 2007, ApJ, 667, 760

Zhu, G., Zheng, Z., Lin, W. P., Jing, Y. P., Kang, X., & Gao, L. 2006, ApJ, 639, L5

Zu, Y., Zheng, Z., Zhu, G., & Jing, Y. P. 2008, ApJ, 686, 41